Performing SU(d) Operations and Rudimentary Algorithms in a Superconducting Transmon Qudit for $d = 3$ and $d = 4$

Pei Liu,[1,*] Ruixia Wang,[2] Jing-Ning Zhang,[2,†] Yingshan Zhang,[2] Xiaoxia Cai,[2] Huikai Xu,[2] Zhiyuan Li,[2] Jiaxiu Han,[2] Xuegang Li,[2] Guangming Xue,[2] Weiyang Liu,[2,‡] Li You,[1,2,3] Yirong Jin,[2] and Haifeng Yu[2]

[1]*State Key Laboratory of Low-Dimensional Quantum Physics, Department of Physics, Tsinghua University, Beijing 100084, China*

[2]*Beijing Academy of Quantum Information Sciences, Beijing 100193, China*

[3]*Frontier Science Center for Quantum Information, Beijing 100184, China*

(Received 19 October 2022; accepted 3 April 2023; published 23 May 2023)

Quantum-computation architecture based on d-level systems, or qudits, has attracted considerable attention recently due to their enlarged Hilbert space. Extensive theoretical and experimental studies have addressed aspects of algorithms and benchmarking techniques for qudit-based quantum computation and quantum-information processing. Here, we report a physical realization of a qudit with up to four embedded levels in a superconducting transmon demonstrating high-fidelity initialization, manipulation, and simultaneous multilevel readout. In addition to constructing SU(d) operations and benchmarking protocols for quantum-state tomography, quantum-process tomography, randomized benchmarking, etc., we experimentally carry out these operations for $d = 3$ and $d = 4$. Moreover, we perform prototypical quantum algorithms and observe outcomes consistent with expectations. Our work will hopefully stimulate further research interest in developing manipulation protocols and efficient applications for quantum processors with qudits.

DOI: 10.1103/PhysRevX.13.021028

Subject Areas: Quantum Physics, Quantum Information

I. INTRODUCTION

Quantum-computational advantage is largely enabled by the exponentially growing Hilbert space for storing and processing of information. In the most commonly discussed architecture, the basic unit is a two-level system forming a qubit with the computation space growing as 2^N for N qubits. This exponential scaling can be further extended to d^N by introducing qudits, i.e., quantum d-level systems, as basic computational units [1,2]. Such an expanded Hilbert space can be realized without increased hardware complexity in popular quantum-computation platforms [3,4]. In addition to a larger Hilbert space and saved hardware resources, other potential advantages of qudits have also attracted considerable research interest. For example, the accuracy and efficiency of simple quantum circuits and algorithms can be enhanced by qudit-based architecture [5]. Quantum simulation can enjoy the flexibility of qudits, with which the many-body Hamiltonian can be encoded directly for simulating higher-spin systems [6], such as bosonic spin-1 models with $d = 3$. In quantum-nonlocality-based information processing, the qudit also plays an important role by helping to close out the detection loophole often tormenting Bell test experiments [7,8]. In quantum-key distribution, the qudit can lead to increased security and a higher key rate [9], and with the qudit as a quantum repeater, an improved communication scheme is possible [10].

Implementations of qudits have been studied on various physical platforms. For trapped ions with multilevels, an experimental realization was reported recently [11]. A universal operation set for implementing qudit-based computation, including state preparation, single-qudit gates, two-qudit gates, and measurement schemes has been provided [3,12]. Qudits based on multilevel atom arrays are employed to explore dipole-dipole interactions [13]. For photonic systems, a variety of inherent properties of a photon, including its orbital angular momentum [14], frequency bin [15,16], time bin [17,18], and path [5], have been used to construct qudits. Moreover, qudit-based quantum computation is studied in continuous spin systems [19], nitrogen-vacancy centers in diamond [20], and nuclear-magnetic-resonance (NMR) systems [21,22].

*liu-p20@mails.tsinghua.edu.cn

†zhangjn@baqis.ac.cn

‡liuwy@baqis.ac.cn

In recent years, qubit-based superconducting quantum-computation (SQC) research has witnessed significant progress in quantum machine learning [23], quantum chemistry [24,25], quantum simulation [26], quantum error correction [27], and quantum-computational advantage with more than 50 qubits [28], etc., with the transmon as a favored physical realization due to its insensitivity to charge noise [29]. Because of its tunable multilevel structure, a superconducting transmon is naturally made for implementing a qudit, and investigating the manipulations of higher-excited states has become a significant priority to realize qudit-based architecture for quantum-information processing. In qubit-based SQC where quantum information is encoded in a computational space unit spanned by the lowest two levels, higher-excited states also play a non-negligible role in the implementation of quantum operations, such as the two-qubit gate [30–32] and shelving readout [33,34] protocols.

Recently, employing superconducting transmon qudits as basic units for quantum-information processing has attracted increased attention, with quantum information encoded into an expanded Hilbert space augmented by higher-excited states. Operational protocols for universal gates and algorithms have been explored theoretically for the transmon qudit [35]. However, most earlier studies focused on qutrit manipulation for $d = 3$ [36–42] or simulation for $d = 4$ [43], limited by the nature of the transmon. The coherence time of higher-excited states decreases as the number of excitations increases, approximately proportional to $1/m$ with m labeling the number of excitations [44]. The charge-parity effect, which often manifests itself as a beat note in the Ramsey interference, causes an increased frequency dichotomy for higher levels [44,45], and hence undermines precise manipulations through frequency addressing or phase correction. The implementation of qudit-based architecture thus calls for stricter requirements on the quality of the transmon device. Specifically, it requires the transmon to have a longer coherence time and weaker charge-parity effect. When both of these requirements are fulfilled, as it is for the device used in our experiment, the advantages of qudits emerge. In addition, the ability to simultaneously discriminate multiple states also contributes to high-fidelity implementation.

This work implements high-fidelity qudit manipulations for $d = 3$ and $d = 4$ in a specifically designed and fabricated superconducting transmon exhibiting long coherence time and weak charge-parity effect. We accomplish simultaneous four-state readout with fidelity above 91.1% for each state. To benchmark the performance, we prepare and measure a four-level state with fidelity of 99.64% and experimentally estimate the error per gate as $(7.6 \pm 0.1) \times 10^{-4}$ $[(1.5 \pm 0.1) \times 10^{-3}]$ for $\pi/2$ pulses between levels $\{|1\rangle, |2\rangle\}$ ($\{|2\rangle, |3\rangle\}$). We also implement several rudimentary algorithms to show the efficacy and efficiency of the single-qudit processor. Our experiments demonstrate the feasibility of encoding and processing more than one bit of quantum information in a single superconducting transmon, and we hope it will stimulate more interest in theoretical and experimental studies of the qudit-based quantum-information-processing architecture.

This paper is arranged as follows. First, the arbitrary SU(d) operation construction with its physical realization and common benchmarking protocols, such as quantum-state tomography [36,46], quantum-process tomography, and randomized benchmarking [3] are discussed in Sec. II. Then, the discrete Fourier-transform algorithm, Grover's algorithm, and the variational quantum-eigensolver algorithm in quantum chemistry are implemented in our qudit system as applications in Sec. III. We end with a conclusion and outlook in Sec. IV.

II. GATE DESIGN AND BENCHMARKING

In this section, we describe the gate decomposition theory and the relevant protocols for benchmarking. We cover the construction protocols for SU(d) operations with their physical realizations in a transmon qudit in Sec. II A and the protocols for quantum-state tomography, quantum-process tomography, and randomized benchmarking in Sec. II B.

A. Construction of SU(d) operations

Microwave-driven transitions can drive a qudit, connecting levels in a quantum system as in trapped-ion system or a superconducting one, etc., with designated single- or multiphoton transitions to perform qudit manipulations. Between any two d levels, the coupled transition provides a universal form

$$\hat{R}_{m,n}(\theta,\phi) = \exp\left[-\frac{i\theta}{2}(\cos\phi\hat{\sigma}_x^{m,n} + \sin\phi\hat{\sigma}_y^{m,n})\right] \quad (1)$$

of rotation, with $\hat{\sigma}_x^{m,n} = |m\rangle\langle n| + |n\rangle\langle m|$ and $\hat{\sigma}_y^{m,n} = -i|m\rangle\langle n| + i|n\rangle\langle m|$. Here, $|m\rangle$ and $|n\rangle$ with $m, n = 0, 1, \ldots, d-1$ and $m \neq n$ are arbitrary basis states of the d-level qudit. With $\hat{R}_{m,n}(\theta,\phi)$, the transitions that cannot be directly implemented are constructed from a combination of several transitions in sequence, for example,

$$\hat{R}_{m,m+2}(\theta,\phi) = \hat{R}_{m,m+1}(-\pi,\phi_1) \times \hat{R}_{m+1,m+2}(\theta,\phi_2)\hat{R}_{m,m+1}(\pi,\phi_1), \quad (2)$$

with $\phi_1 + \phi_2 - \pi/2 = \phi$, i.e., from first swapping the amplitudes between $|m\rangle$ and $|m+1\rangle$, then carrying out the rotation operation between $|m+1\rangle$ and $|m+2\rangle$, and finally, swapping the amplitudes for $|m+1\rangle$ and $|m\rangle$ back. To simplify the above composite operation, we typically choose $\phi_2 = \phi$ and $\phi_1 = \pi/2$ as a symmetric and standard protocol. Whenever $\hat{R}_{m,n}(\theta,\phi)$ precedes another rotation $\hat{R}_{m,n}(\theta',\phi')$ on the same two levels, it is convenient to

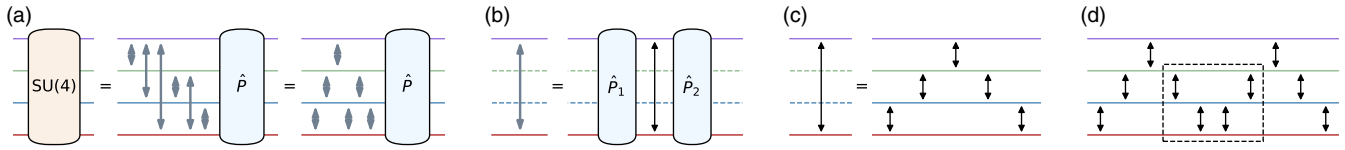

FIG. 1. A circuit diagram illustration for arbitrary unitary operations on a four-level system. (a) The Gaussian elimination method decomposes an SU(4) operation into a sequence of SU(2) operations plus a generalized phase gate, as in normal or bubbling Gaussian elimination. Here, gray arrows represent SU(2) operations in a subspace spanned by any two levels. (b) Such SU(2) operations can be constructed by two generalized phase gates with a two-level rotation operation $\hat{R}_{m,n}(\theta,\phi)$ sandwiched in between. Black arrows represent transitions between two levels with a microwave drive. (c) The arbitrary rotation $\hat{R}_{m,n}(\theta,\phi)$ can be realized by direct multiphoton coupling, or a sequence of transitions between adjacent levels without crossing to nonadjacent ones. (d) If a transition $\hat{R}_{m,n}(\theta',\phi')$ follows another $\hat{R}_{m,n}(\theta,\phi)$ in the same two-level subspace, some auxiliary adjacent transitions according to Eq. (2), as shown in the black dashed box, can be neglected at all times, which constitutes a straightforward strategy to simplify circuit.

eliminate some constituting pulses in the sandwiched structure of Eq. (2) to simplify the total sequence.

Besides microwave-driven transitions, the generalized phase gate defined as $\hat{P}(\vec{\Phi})=\sum_k \exp(i\phi_k)|k\rangle\langle k|$ is another important repertoire for qudit manipulation. It can be realized by $3(d-1)$ resonant pulses according to Ref. [3]. Often it gets too complicated, particularly when it appears in the middle of a sequence as an independent unitary operation. Inspired by the idea of a virtual Z gate from qubit control [47] and noting that

$$\hat{R}_{m,n}(\theta,\phi)\hat{P}(\vec{\Phi})=\hat{P}(\vec{\Phi})\hat{R}_{m,n}(\theta,\phi+\phi_m-\phi_n), \quad (3)$$

we find that one can swap the generalized phase gate from arbitrary positions of a circuit to the very beginning, and then ignore it, as with the virtual Z gate [47]. Such a virtual operation requires zero time; hence, it can be executed perfectly. With such a generalized virtual phase gate, operation sequences can be further simplified. An arbitrary SU(2) operation can then be constructed effectively as in the following:

$$\hat{U}_2^{m,n}(\theta,\phi,\lambda,\delta)=\hat{P}(\vec{\Phi}^{(1)})\hat{R}_{m,n}\left(\theta,\frac{\pi}{2}\right)\hat{P}(\vec{\Phi}^{(2)}),$$
$$\phi_k^{(1)}=\begin{cases}-\frac{\lambda}{2}, & k=m,\\ \frac{\lambda}{2}, & k=n,\\ 0, & \text{otherwise},\end{cases}$$
$$\phi_k^{(2)}=\begin{cases}\delta-\frac{\phi}{2}, & k=m,\\ \delta+\frac{\phi}{2}, & k=n,\\ 0, & \text{otherwise}.\end{cases} \quad (4)$$

The actual decomposition of an arbitrary unitary operation on a d-level qudit into a sequence of unitary operations on two-level subsystems follows the idea of Gaussian elimination [48–50]. An SU(d) operation can normally be expressed as a unitary matrix of order d, and the Gaussian elimination algorithm takes this matrix as input and outputs a sequence of SU(2) operations between various pairs of the d levels, or simply expressed as in the following:

$$\hat{U}_d^{0,1,\ldots,d-1}=\hat{P}(\vec{\Phi})\hat{U}_2^{m_k,n_k}\cdots\hat{U}_2^{m_1,n_1}\hat{U}_2^{m_0,n_0}, \quad (5)$$

where a total of $(k+1)$ SU(2) operations are required in a given order and $m_l,n_l\in\{0,1,\ldots,d-1\}, l=0,1,\ldots,k$. There are two strategies of Gaussian elimination. The normal one and the bubbling one are described in Algorithms 1 and 2, respectively. Figure 1 illustrates the decomposition process for $d=4$. With the abovementioned protocol, an arbitrary SU(d) operation can be constructed based on two-level ones.

As for experiments, our qudit system is constructed with a superconducting transmon [29], whose Hamiltonian can be expressed as $\hat{H}=4E_C(\hat{n}-n_g)^2-E_J\cos\hat{\phi}$ with E_c the charging energy and E_J the Josephson energy. For suitable parameters, several bound states exist in the cosine potential well, as shown in Fig. 2(a). The anharmonicity of the cosine potential for the qudit ensures that the transition frequencies between any two energy levels are different. Several single- or two-photon transitions are shown in Fig. 8 with specific parameters for our device in Table I. It is easy to find that for adjacent transitions, or transitions

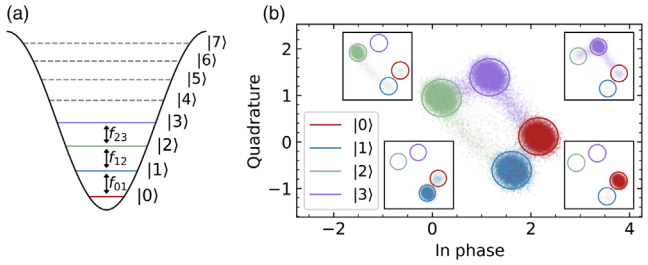

FIG. 2. Qudit-level diagram and readout calibration. (a) The quantum state is encoded as a superposition of several bound levels in a cosine potential well labeled by $|0\rangle$, $|1\rangle$, $|2\rangle$, and $|3\rangle$. Higher levels on this device are plotted as gray dashed lines. (b) The quadrature representation of readout benchmarking, with fidelities $P_0=99.1\%$, $P_1=94.5\%$, $P_2=94.5\%$, and $P_3=91.1\%$. The qudit is prepared in $|k\rangle$ with a possible global phase and measured in $|k\rangle$ with a probability P_k.

TABLE I. Error of gates.

SU(d)	Levels	Clifford	$\pi/2$ pulse
SU(3)	$\{0,1,2\}$	$(5.4\pm0.1)\times10^{-3}$	$(1.02\pm0.02)\times10^{-3}$
SU(4)	$\{0,1,2,3\}$	$(5.8\pm0.2)\times10^{-2}$	$(4.1\pm0.1)\times10^{-3}$
SU(2)	$\{0,1\}$	$(4.6\pm0.3)\times10^{-4}$	$(2.1\pm0.1)\times10^{-4}$
SU(2)	$\{1,2\}$	$(1.7\pm0.1)\times10^{-3}$	$(7.6\pm0.1)\times10^{-4}$
SU(2)	$\{2,3\}$	$(2.3\pm0.1)\times10^{-3}$	$(1.5\pm0.1)\times10^{-3}$

between neighboring levels of a transmon, a shorter evolution time is needed than for two-photon ones due to stronger single-photon couplings. To suppress the charge-parity effect, E_J/E_c is designed to take a large ratio ($E_J/E_C\approx88$) compared to the usual values.

The transmon qudit is coupled to a readout resonator, whose frequency responds differently when the qudit is prepared in different states, facilitating simultaneous readout of the qudit directly. As shown in Fig. 2(b), the first four states labeled $|0\rangle$, $|1\rangle$, $|2\rangle$, and $|3\rangle$ can be distinguished with high fidelity. The details on the readout can be found in Appendix C.

Taking into consideration both the energy-level structure and readout fidelity, we can implement a qudit system of $d\le4$ with three transitions on neighboring levels over a short operation time, although two-photon transitions as well as the fifth state $|4\rangle$ ($d=5$) remain observable, which would likely increase our ability to manipulate for $d>4$ in the future. The beat frequency of the Ramsey interference between $|2\rangle$ and $|3\rangle$ is less than 0.1 MHz, and thus impairs only the manipulations slightly which constitutes the key reason for our success in the high-fidelity SU(4) manipulations. At the same time, if we choose the bubbling Gaussian elimination instead, which is the most suitable for the qudit under discussion, no more than $d(d-1)/2$ operations are needed, resulting in at most $d(d-1)$ $\pi/2$ pulses and a complexity of $\mathcal{O}(d^2)$ that is close to the theoretical limit. Mathematically, the Gaussian elimination is not restricted to a specific elimination order. In other words, both the normal one and the bubbling one can fulfill the same goal, but the order of elimination, or the elimination strategies, exhibit different complexities in a specific quantum system depending on the level structure. We choose normal Gaussian elimination which is widely known and general in this work, leading to a complexity of $\mathcal{O}(d^3)$, when an arbitrary SU(2) operation has to be expanded in terms of adjacent SU(2) transitions. This strategy avoids optimizations in the ladder system than the bubbling strategy, especially in the present system, consistent with our motivation for a universal demonstration.

B. Quantum-state tomography, quantum-process tomography, and randomized benchmarking

Quantum-state tomography (QST) is a standard method for determining the density matrix of a state. Here we follow the multilevel QST protocol developed in a NMR system [46] and a superconducting transmon qutrit [36]. With the readout process presented in Sec. II A, only the diagonal elements of density-matrix operator $\hat\rho$ can be accessed. To measure an arbitrary density-matrix element of a qudit, several operations for swapping off-diagonal elements to linear combinations of the diagonal ones are needed before measurement. For $d=4$, we apply a total of 12 operations $\hat M_l, l=0,1,\ldots,11$ (listed in Appendix D) before measurement, and the measured probabilities are $P_{l,k}=\langle k|\hat M_l^\dagger\hat\rho\hat M_l|k\rangle$ with $l=0,1,\ldots,11$ and $k=0$, 1, 2, 3, and $\sum_k P_{l,k}=1$. An overdetermined group of equations can then be derived, whose solution gives the unknown $\hat\rho$. According to the properties of the density matrix, the maximum likelihood estimation (MLE) [51,52] with the simple estimation of $\hat\rho$ from Eq. (D2) taken as the initial guess, reduces the impact of other undesirable errors on the output density matrix. Figure 3 displays QST measurement results for a superposition state $|\psi\rangle=(1-i)|0\rangle/\sqrt{8}+|1\rangle/\sqrt{2}-(1+i)|2\rangle/\sqrt{8}$, finding $\hat\rho=|\psi\rangle\langle\psi|$ with a high 99.64% fidelity. For dimensions with $d>4$, we can construct an analogous measurement operator. For $d=3$, we can simply truncate the above $d=4$ protocol.

Quantum-process tomography (QPT) is based on QST [3,49]. It provides a convenient measure to characterize a quantum process. Similar to QPT for a qubit, we initialize our qudit in a set of given states, then apply the process we want to determine, and at the end of the process, we carry out QST to measure the final state. For a quantum process represented by

$$\hat\rho_f=\sum_{k,l}\hat\lambda_k\hat\rho_i\hat\lambda_l^\dagger\chi_{k,l}, \tag{6}$$

with initial (final) state $\hat\rho_i(\hat\rho_f)$, λ_l ($l=0,1,\ldots,d^2-1$) is the identity matrix or d^2-1 generators of the SU(d) group,

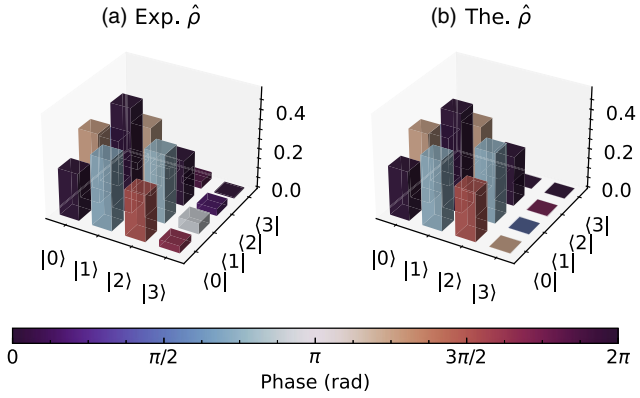

FIG. 3. Quantum-state tomography with the MLE for the state $|\psi\rangle=(1-i)|0\rangle/\sqrt{8}+|1\rangle/\sqrt{2}-(1+i)|2\rangle/\sqrt{8}$ in the four-level qudit, where (a) shows the experimental results and (b) shows the expected theoretical ones. The height of each bar represents the amplitude, while color represents the phase. The corresponding state fidelity is 99.64%.

corresponding to the operator $\hat{\lambda}_l$ (details of its construction are available in Algorithm 3). In particular, when $d = 3$, the matrices $\lambda_1, \lambda_2, \ldots, \lambda_8$ are known as the Gell-Mann matrices. Under this basis, the superoperator $\hat{\chi}$ (corresponding to matrix representation $\{\chi_{k,l}\}$) has desirable properties to guarantee the MLE in solving the overdetermined group of equations for QPT. As an example, benchmarking of the discrete Fourier transformation is illustrated in Sec. III.

Randomized benchmarking (RB) on three-level and four-level systems can be used to estimate average gate errors, just like the RB sequence on a qubit [3]. We note that Clifford gate groups for a qudit are different from that for a single qubit. Specifically, there are 216(768) group elements for the $d = 3(4)$ qudit (see Appendix F for more details). We translate the matrix representations of Clifford elements into executable sequences of $\pi/2$ pulses. The average number of $\pi/2$ pulses required to apply the Clifford gate in the three-dimensional Clifford group $\mathcal{C}_3$ and four-dimensional Clifford group $\mathcal{C}_4$ are $1134/216 = 5.25$ and $10976/768 \approx 14.292$, respectively. The experimental results are shown in Figs. 4 and 11, with a summary of errors shown in Table I. We find the average errors calculated from the SU(3) and SU(4) Clifford groups are larger than those from SU(2).

Several explanations are now in order to help understand the situation. First, higher levels in a transmon typically exhibit a shorter energy relaxation time, implicating more incoherent errors. In other words, the upper bound of fidelity decreases as the energy level becomes higher [53], consistent with the decreasing RB fidelity we observe as the subspace expands to include higher levels. The charge-parity effect becomes worse at higher levels as well, and the associated frequency dichotomy causes phase uncertainty. Second, leakage is regarded as an incoherent error in a two-level system, whereas it is a coherent error sometimes in multilevel cases. In the latter case, RB is insensitive to such an error, leading to the situation where the $\pi/2$ pulse error calculated from RB in $\mathcal{C}_3$ or $\mathcal{C}_4$ is larger than that from $\mathcal{C}_2$; thus, more refined leakage control for $d = 3$ and 4 is needed. Both energy relaxation and frequency bandwidth with finite-time drive pulses contribute to the leakage error beyond the two-level subspace. From Fig. 11, we can find an obvious leakage error. As a result, the level population does not converge to the expected value after evolving for a sufficiently long time. Transition frequency crowding makes the leakage error worse, because the adjacent transition frequency between $|1\rangle$ and $|2\rangle$ is naturally close to the three-photon transition frequency between $|0\rangle$ and $|3\rangle$. If the amplitude of the driving pulse between $|1\rangle$ and $|2\rangle$ is large enough, the frequency bandwidth for a finite-time driving pulse needs to be carefully modified to avoid three-photon transitions. Finally, due to the averaging effect of the RB sequence, specific types of errors such as non-Markovian errors in operations [54,55] could not be observed, and only limited manipulation errors can be detected, leading to decreased realized manipulation fidelity. Analyzing the sources of the abovementioned errors is of great importance for improving the manipulation accuracy, and the limit to which this can be achieved depends on the development of the required theoretical tools in the future.

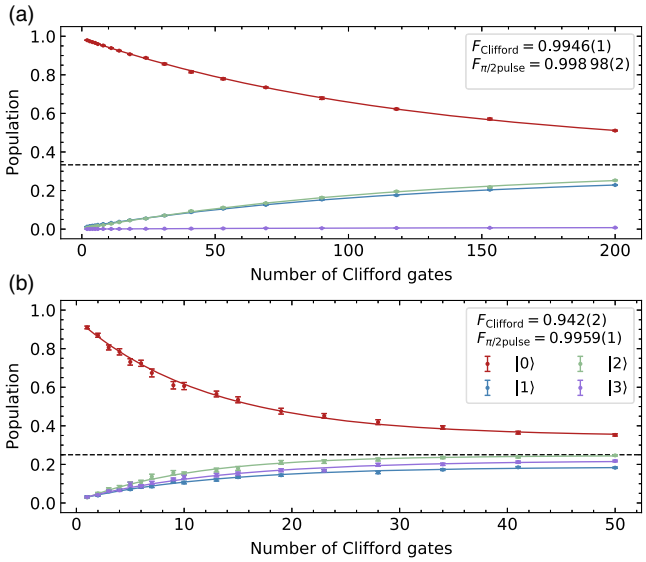

FIG. 4. Randomized benchmarking for (a) three-level and (b) four-level qudits. We initialize the qudit in $|0\rangle$, then apply a certain extra number of Clifford gates from the (a) three-dimensional Clifford group $\mathcal{C}_3$ (involving $|0\rangle$, $|1\rangle$, and $|2\rangle$) and the (b) four-dimensional Clifford group $\mathcal{C}_4$ (involving $|0\rangle$, $|1\rangle$, $|2\rangle$, and $|3\rangle$), and finally, we add a Clifford gate to ensure that the total sequence is equivalent to the identity. Populations of the four states $|0\rangle$, $|1\rangle$, $|2\rangle$, and $|3\rangle$ are measured simultaneously in the end, which are shown as crosses with error bars and corresponding colors. Solid lines with corresponding colors show the exponential fits according to the theory of RB. $\pi/2$ pulses with an average number of $A_3 = 5.25$ are used in $\mathcal{C}_3$ and an average number of $A_4 = 14.292$ in $\mathcal{C}_4$, which give the average calculated fidelities of $\pi/2$ pulses as $F_{\pi/2\text{pulse}} = 1 - (1 - F_{\text{Clifford}})/A_k, k = 3, 4$. Black dashed lines indicate the populations of a mixed state after a sufficiently long evolving time.

III. APPLICATIONS

In this section, we present three quantum algorithms that are performed to demonstrate the capabilities of our transmon qudit. The benchmarking methods QST and QPT are employed to verify the relevant processes for the respective algorithms. The experimental results are found to be in nice agreement with theories, and they illustrate the high efficiency and accuracy of our four-level transmon manipulations.

A. Discrete Fourier transformation and cyclic permutation parity check

The first application we perform is the parity check of cyclic permutations using discrete Fourier transformation

(DFT). It has been studied in NMR before [56] with the circuit diagram as shown in Fig. 5(a). To check for a permutation of length d, the qudit is initialized into a coherent superposition state $\mathrm{DFT}_d|m\rangle$, $m=0,1,2,\ldots,d-1$. Then, the permutation operation $\hat{U}_k, k=1,2,\ldots,d!$ is applied. Before measurement, an inverse DFT labeled by DFT^{-1} is applied to transform the state into the final one. A different final state would indicate different parity of the cyclic permutation.

Here the process of DFT is implemented via the normal Gaussian elimination decomposition, which translates the matrix representation DFT_d into a sequence of SU(2) operation pulses, with matrix element $\mathrm{DFT}_d(j,k)$ in row j and column k taking the form

$$\mathrm{DFT}_d(j,k)=\frac{1}{\sqrt{d}}e^{2ijk\pi/d}, \qquad j,k=0,1,\ldots,d-1. \tag{7}$$

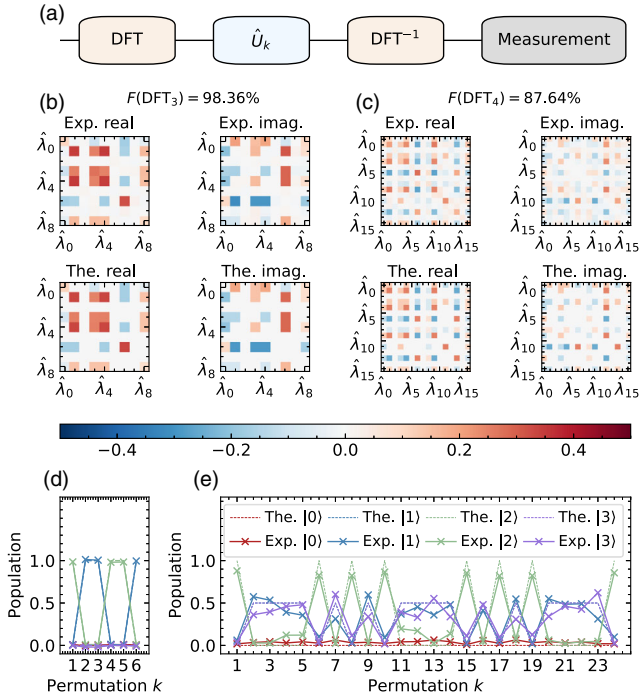

FIG. 5. Discrete Fourier transformation and parity check of cyclic permutation. (a) The qudit is initialized into a superposition state, and the unitary permutation operation is followed by the inverse DFT and readout. Quantum-process tomography of (b) DFT_3 and (c) DFT_4 shows fidelities of 98.36% and 87.64%, respectively. Results for each permutation k (d) for $d=3$ and (e) for $d=4$ with initial state $|2\rangle$ prepared, where dashed lines denote theoretical expectations, while crosses show total experiment outputs. Different colors show the projection measurement results for different states at the same time. The consistency of the measured population and theoretical distribution affirms the reliable construction of arbitrary unitary operation in the transmon qudit, though the success of the parity-checking algorithm depends on the choice of the initial-state preparation. Experimental (theoretical) results in (b)–(e) are labeled by Exp. (The.), while the real (imaginary) parts are labeled by real (imag.).

The operations of DFT_3 and DFT_4 are benchmarked by QPT. Figures 5(b) and 5(c) show the corresponding results, which give their respective fidelities of $\mathcal{F}(\mathrm{DFT}_3)=98.36\%$ and $\mathcal{F}(\mathrm{DFT}_4)=87.64\%$.

$\hat{U}_k$, the permutation operator of length d, is given by

$$\hat{U}_k=\begin{bmatrix}0 & 1 & \cdots & d-1\\ p_{k,0} & p_{k,1} & \cdots & p_{k,d-1}\end{bmatrix}, \tag{8}$$

with $\hat{U}_k|j\rangle=|p_{k,j}\rangle$, where $p_{k,j}\in\{0,1,\ldots,d-1\}$, $\forall\, j\in\{0,1,\ldots,d-1\}$, and $\forall\, j_1\neq j_2, p_{k,j_1}\neq p_{k,j_2}$ for k in an ascending lexicographical order of $p_{k,1}, p_{k,2}, \ldots, p_{k,d}$. The simplest construction of $\hat{U}_k$ uses no more than $d(d-1)/2$ π pulses according to the properties of the permutations, which constitute an example of pulse sequence optimization for specific operations according to their properties. More details are provided in Appendix G 2.

It is worth noting that the choice of the initial state affects the result of this algorithm with $m=0$ being the trivial case and neglected. When m and d are coprime numbers, i.e., $\gcd(m,d)=1$, the parity of the cyclic permutation can be directly obtained from the measurement result of the populations for $|m\rangle$ and $|d-m\rangle$. The $|m\rangle$ state indicates even parity, and the $|d-m\rangle$ state affirms odd parity. If other initial states are chosen, the results would be a bit complicated. Suppose $C_{d,\mathrm{even(odd)}}$ is an arbitrary cyclic permutation of even (odd) parity with length d, and the permutation set $\mathcal{G}(m,d)$ is a subgroup of a permutation group $\mathcal{C}(d)$ with length d, which depends only on m and d (more construction details are given in Appendix G 1). If a permutation $\hat{U}_k$ is recognized by the population of state $|m\rangle$ during readout, it satisfies

$$\hat{U}_k\in\bigcup_{g\in\mathcal{G}(m,d)} gC_{d,\mathrm{even}}, \tag{9}$$

while the readout population of state $|d-m\rangle$ corresponds to $C_{d,\mathrm{odd}}$ with $d=2m$ a special case for which both even and odd permutations give the same readout.

An earlier experiment [56] reported the case of $d=4$, $m=1$. Here, other choices such as $d=3$, $m=2$ and $d=4$, $m=2$ are studied, with the results, respectively, displayed in Figs. 5(d) and 5(e). The parity-check algorithm for the former case is confirmed, whereas it is not completely established for the latter, as the result recognizes the cyclic permutation from the whole permutation set but fails in the parity check. However, the fidelities from QPT of DFT operations and the high consistency between the measured populations and theoretical distribution of the circuit show that arbitrary unitary operations within the transmon qudit are realizable.

B. Grover's algorithm

Next, we discuss the implementation of Grover's algorithm [57,58] in a four-level quantum system, where each

level represents an item in an unsorted database. The goal is to locate a specific item labeled by an oracle operation, a black-box operation that has nontrivial effect only on the labeled level. Without loss of generality, we choose the oracle operation $\hat{P}_{\text{label}}$ such that the amplitude of the labeled level $|\text{label}\rangle$ flips its sign or acquires an $e^{i\pi}$ phase.

The first four levels of our transmon qudit are used, and the operation $\hat{H}$ for initialization carries out $\hat{H}|0\rangle = 1/2\sum_{n=0}^{3}|n\rangle$ with the matrix representation H taking the form

$$H = \frac{1}{2}\begin{pmatrix} 1 & 1 & 1 & 1 \\ 1 & -1 & 1 & -1 \\ 1 & 1 & -1 & -1 \\ 1 & -1 & -1 & 1 \end{pmatrix}, \tag{10}$$

which is the same as the generalized Hadamard operator. It turns into an equal superposition of all basis states and with the oracle marking the specific state for Grover's algorithm to find through a generalized phase gate $\hat{P}_{\text{label}}(\vec{\Phi})$ satisfying

$$\phi_j = \begin{cases} -1, & j = \text{label}, \\ 1, & \text{otherwise}. \end{cases} \tag{11}$$

The simplest search operator $\hat{G}$ takes the form

$$G = \frac{1}{2}\begin{pmatrix} -1 & 1 & 1 & 1 \\ 1 & -1 & 1 & 1 \\ 1 & 1 & -1 & 1 \\ 1 & 1 & 1 & -1 \end{pmatrix}. \tag{12}$$

For most instances, the search operator would be more complicated, because an arbitrary phase rotation satisfying the phase-matching requirement is needed to achieve an accurate search [59]. But for $d = 4$, this phase is just π, and therefore $\hat{G}$ takes the original form. At the end of the search operation, we measure the qudit to affirm the state. Figure 6(a) shows the complete gate sequence.

The labeled state is read with data shown in Fig. 6(b) in red, blue, green, and purple colors for $|0\rangle$, $|1\rangle$, $|2\rangle$, or $|3\rangle$ being labeled, respectively. From these results, we obtain a trained dataset $\langle X_n\rangle = \sum_m mP_m(n)$ where $P_m(n)$ denotes the probability of reading out $|m\rangle$ in 4096 runs when we label state $|n\rangle$ with a standard deviation $\Delta\langle X_n\rangle$ from 25 repetitions. $\langle X_n\rangle \pm \Delta\langle X_n\rangle, n = 0, 1, 2, 3$ provides an identification confidence interval. One-hundred random test results are plotted as black crosses in Fig. 6(c), which fits well with the range from training and confirms accurate manipulation in the qudit and the reliable execution of the decomposed sequence for universal SU(d) operations.

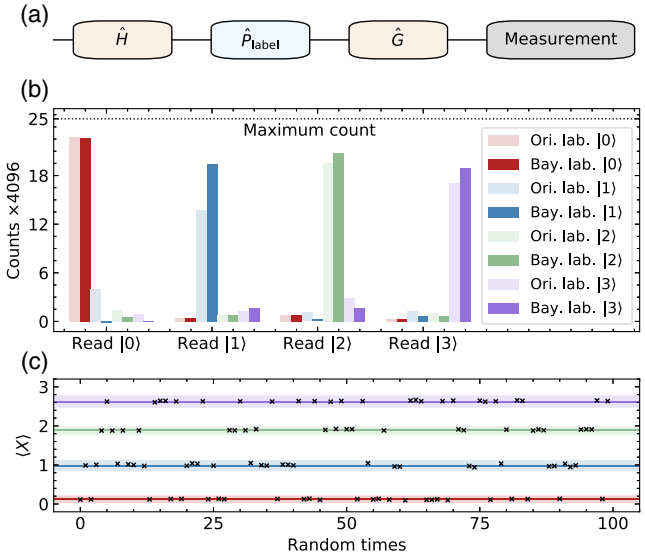

FIG. 6. Grover's algorithm. (a) The circuit with qudit initialized by a Hadamard operation into an equal superposition state, followed by an oracle that labels one of the basis states, and a standard $\hat{G}$ operation applied with measurement in the end. (b) Training for the labeled state and readout results. We label $|0\rangle$, $|1\rangle$, $|2\rangle$, and $|3\rangle$ in the Grover circuit and collect all measurement results shown in different colors, respectively. For each labeled state, 25×4096 runs are tested and displayed in the form of a histogram, and the light colors show original counts while dark colors show counts after Bayesian correction. The dotted line indicates the maximum count, which is the theoretical value without any error channel. (c) A simple test with a random labeled state. For each test, the expectation $\langle X\rangle$ is calculated from 4096 runs. They are remarkably differentiated from each other, and the shadow shows the standard deviation trained from (b) with corresponding color.

C. Variational quantum eigensolver in quantum chemistry

Quantum-chemistry calculation or quantum-chemistry simulation is a popular application for quantum-information processing. In the noisy intermediate-scale quantum era, a quantum algorithm like the variational quantum eigensolver (VQE) attracts a lot of attention [60,61], and several experiments have implemented VQE in qubit systems, solving for ground-state H_2 energy in a superconducting system [24] and HeH^+ energy in a trapped-ion system [11]. The dimension of Hilbert space in these two early studies is limited to two qubits or four-level systems, which we can implement (perhaps with higher qualities) in the transmon qudit.

As detailed in Appendix H, to obtain the ground-state energy of H_2, VQE minimizes the encoded Hamiltonian

$$H_{H_2}^{\text{BK}} = a_0 I + a_1 IZ + a_2 ZI + a_3 ZZ + a_4 XX, \tag{13}$$

with a trial wave function $e^{i\theta XY}|11\rangle$, where X, Y, and Z are Pauli matrices of a single qubit, $|11\rangle$ is the Hartree-Fock

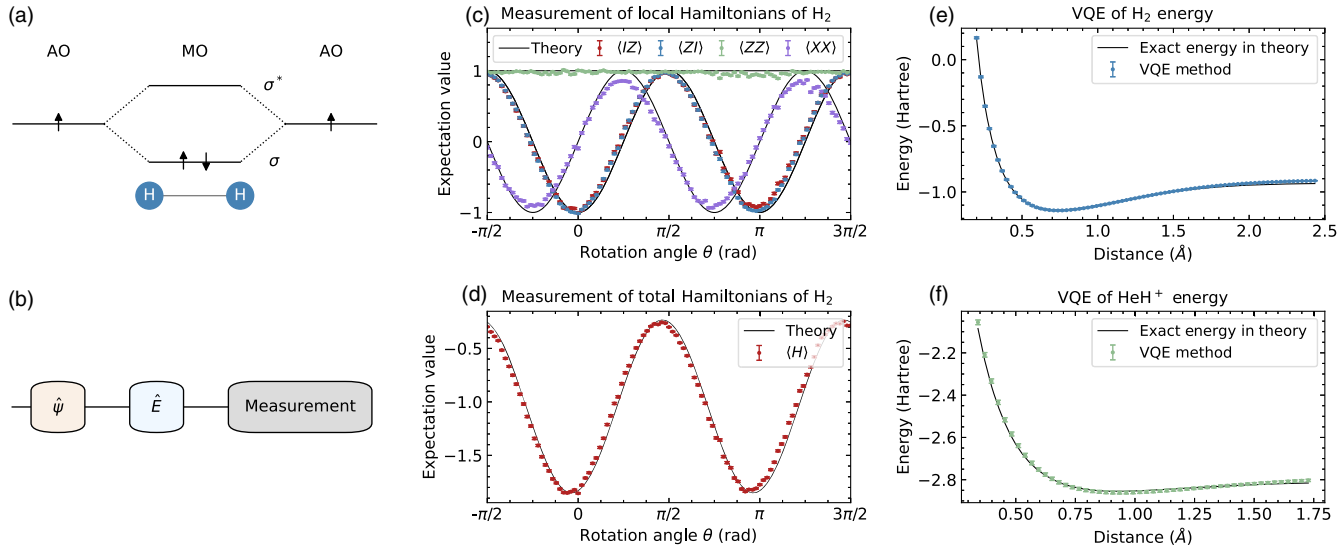

FIG. 7. Solving for H_2 and HeH^+ ground-state energies with VQE. (a) Formation of molecular orbitals for H_2. (b) VQE circuit in the qudit, with a trial initial wave function $\hat{\Psi}$ and a rotation of measurement operator $\hat{E}$. (c) Expectation for each measurement operator for local Hamiltonian in H_2. (d) Hamiltonian of H_2 as a function of the rotation angle θ, the variation parameter of the trial wave function. (e) Energy of the ground state for H_2. (f) Energy of the ground state for HeH^+.

state encoded by Bravyi-Kitaev transformation with Z_2 symmetry, and coefficients $\{a_l\}$ are calculated on a classical computer. When running in four-level system, the two-qubit states are mapped to multilevel states, for instance, choosing $|00\rangle \to |0\rangle$, $|01\rangle \to |1\rangle$, $|10\rangle \to |2\rangle$, and $|11\rangle \to |3\rangle$. The trial wave function $e^{i\theta XY}|11\rangle$ is thus mapped to

$$\begin{aligned} e^{i\theta XY}|11\rangle &\to \hat{P}(\vec{\Phi})\hat{U}^{(4)}\hat{U}^{(3)}\hat{U}^{(2)}\hat{U}^{(1)}\hat{U}^{(0)}|0\rangle, \\ \hat{U}^{(0)} &= \hat{U}_2^{|0\rangle,|1\rangle}\left(\pi, 0, \pi, \frac{\pi}{2}\right), \\ \hat{U}^{(1)} &= \hat{U}_2^{|1\rangle,|2\rangle}\left(\pi, 0, \pi, \frac{\pi}{2}\right), \\ \hat{U}^{(2)} &= \hat{U}_2^{|2\rangle,|3\rangle}\left(\pi, 0, \pi, \frac{\pi}{2}\right), \\ \hat{U}^{(3)} &= \hat{U}_2^{|0\rangle,|3\rangle}\left(2\theta, 0, -\pi, \frac{\pi}{2}\right), \\ \hat{U}^{(4)} &= \hat{U}_2^{|1\rangle,|2\rangle}\left(2\theta, -\pi, 0, \frac{\pi}{2}\right), \\ \vec{\Phi} &= (\pi, \pi, 0, 0)^T \end{aligned} \tag{14}$$

derived from Gaussian elimination in Algorithm 1, which constitutes a precise decomposition. The measurements of $\langle IZ\rangle$, $\langle ZI\rangle$, $\langle ZZ\rangle$, and $\langle XX\rangle$ follow the same experimental method as described before. The whole process is illustrated in Fig. 7(b). Figures 7(c) and 7(d) display the theoretical and experimental results of the local and total Hamiltonians (varying with parameters θ), respectively, at the equilibrium point. Figure 7(e) shows the experimental energy curve of the ground state of H_2 as a function of the internuclear distance, which fits well with the exact value (black line).

HeH^+ can also be simulated despite being more complicated than H_2 from the aspect of simulation. The corresponding trial wave function is chosen as

$$\exp\left[i\frac{\theta_1}{2}(IY + YI) + i\frac{\theta_2}{2}(XY + YX)\right]|11\rangle, \tag{15}$$

and the encoded Hamiltonian takes the form

$$\begin{aligned} H_{\mathrm{HeH}^+}^{\mathrm{BK}} &= a_0 I + a_1 IZ + a_2 IX + a_3 ZI + a_4 XI \\ &\quad + a_5 ZZ + a_6 ZX + a_7 XZ + a_8 XX. \end{aligned} \tag{16}$$

Similar to the case of H_2, both wave-function construction operators at given parameters and measurement operations are represented in matrix forms and decomposed by Gaussian eliminations. The corresponding details are not repeated here. Afterward, VQE for HeH^+ is implemented on our system, and the results of ground-state energy are shown in Fig. 7(f), consistent with the exact energy obtained from theoretical calculations. A second figure for the energy error with fluctuations is shown in Fig. 12. Our experiment replaces two coupling transmon qubits with one transmon qudit, saving crucial hardware resources.

IV. CONCLUSION AND OUTLOOK

We realize a set of operations for readout, calibration, quantum-state and -process tomography, and randomized benchmarking in a qudit constructed from a superconducting

transmon. We further implement three algorithms with the well-benchmarked quantum device and verify their advantages in calculation efficiency and accuracy. It demonstrates resources saving with simpler gate operations than two-qubit gates and a reduction in the hardware requirement.

In the transmon qudit, the coupling strength increases as $\sqrt{m}$, slower than the lifetime scaling of $1/m$ for m excitations, which consequently would erect a level limit in high-fidelity manipulations that can be achieved; thus, the scalability of the qudit system is to be reconsidered. In Ref. [2], a summary of the definitions and properties for various examples of qudit gates are provided, including a two-qudit SWAP gate, which can be implemented by using the controlled-shift gate CX_d satisfying $CX_d|x\rangle|y\rangle = |x\rangle|x+y\rangle$. Within such a framework, it shows that universal and complete operations can be constructed in principle. We are hopeful with the achievement reported here, one can go one step further by implementing two-qudit gates in the future as cross-resonant gates or some other schemes. Meanwhile, advanced calculation schemes, more and improved algorithms, and quantum-simulation theories based on qudit systems are urgently needed.

On the side of hardware implementation for qudit systems, transmons remain a popular choice due to their inherent multilevel structure, which proves convenient for realizing multiqudit quantum devices with slight changes in design. What is more, the scalability of a transmon or other choice devices in a superconducting system provides many benefits for implementing qudits, though higher-quality units are needed.

ACKNOWLEDGMENTS

We appreciate the helpful discussion with Yu Song. This work is supported by the National Natural Science Foundation of China (NSFC) Grant No. 11890704, the Beijing Natural Science Foundation Grant No. Z190012, NSFC Grants No. 12104055, No. 12004042, and No. 12104056, and the Key Area Research and Development Program of Guang Dong Province Grant No. 2018B030326001.

Note added.—Recently, we became aware of several related works on the qudit-based quantum computation, including a study of the beat note in Ramsey interference [62], the two-qutrit gate based on a cross-resonant gate and its application [63], the quantum gate set tomography protocol for a qutrit [64], several algorithms demonstrated on a qutrit processor [65], the gate compilation protocol for qudit-based architecture [66], and the comparison of gate efficiency between the qudit and qubits [67].

APPENDIX A: PROOF OF EXCHANGING A GENERALIZED PHASE GATE

The proof of Eq. (3) is shown below.

$$\begin{aligned}
&\hat{R}_{m,n}(\theta,\phi)\hat{P}(\vec{\Phi})\\
&= \left[\cos\frac{\theta}{2}\hat{I}^{m,n} - i\sin\frac{\theta}{2}(\cos\phi\hat{\sigma}_x^{m,n} + \sin\phi\hat{\sigma}_y^{m,n})\right]\left(\sum_{k=m,n} e^{i\phi_k}|k\rangle\langle k|\right) \oplus \left(\sum_{k\neq m,n} e^{i\phi_k}|k\rangle\langle k|\right)\\
&= \left[\cos\frac{\theta}{2}(|m\rangle\langle m| + |n\rangle\langle n|) - i\sin\frac{\theta}{2}(e^{-i\phi}|m\rangle\langle n| + e^{i\phi}|n\rangle\langle m|)\right]\left(\sum_{k=m,n} e^{i\phi_k}|k\rangle\langle k|\right) \oplus \left(\sum_{k\neq m,n} e^{i\phi_k}|k\rangle\langle k|\right)\\
&= \left(\sum_{k\neq m,n} e^{i\phi_k}|k\rangle\langle k|\right) \oplus \left\{\cos\frac{\theta}{2}(e^{i\phi_m}|m\rangle\langle m| + e^{i\phi_n}|n\rangle\langle n|) - i\sin\frac{\theta}{2}[e^{-i(\phi-\phi_n)}|m\rangle\langle n| + e^{i(\phi+\phi_m)}|n\rangle\langle m|]\right\}\\
&= \left(\sum_{k\neq m,n} e^{i\phi_k}|k\rangle\langle k|\right) \oplus \left(\sum_{k=m,n} e^{i\phi_k}|k\rangle\langle k|\right)\left[\cos\frac{\theta}{2}(|m\rangle\langle m| + |n\rangle\langle n|) - i\sin\frac{\theta}{2}(e^{-i\phi'}|m\rangle\langle n| + e^{i\phi'}|n\rangle\langle m|)\right]\\
&= \hat{P}(\vec{\Phi})\hat{R}_{m,n}(\theta,\phi+\phi_m-\phi_n),
\end{aligned} \tag{A1}$$

with $\phi' = \phi + \phi_m - \phi_n$. Therefore, it is valid to swap a generalized phase gate with any arbitrary transition, leading to zero duration of the generalized phase gate, as in the virtual Z strategy [47] discussed before.

APPENDIX B: ALGORITHM FOR GAUSSIAN ELIMINATION

Based on the Gaussian elimination, an arbitrary SU(d) operation can be decomposed into a sequence of SU(2) operations [49,50]. This algorithm takes the unitary d-dimensional matrix representation of the SU(d) operators as input, and outputs an SU(2) operation sequence with generalized phase gates, or simply expressed as the following:

$$\hat{U}_d^{0,1,\ldots,d-1} = \hat{P}(\vec{\Phi})\hat{U}_2^{m_k,n_k}\cdots\hat{U}_2^{m_1,n_1}\hat{U}_2^{m_0,n_0}, \tag{B1}$$

where a total of $(k+1)$ SU(2) operations are required in a given order, and $m_l, n_l \in \{0,1,\ldots,d-1\}, l = 0,1,\ldots,k$.

Algorithm 1. Normal Gaussian elimination decomposition of SU(d).

```
Function GED(d, U):
    Input: current dimension d and the d × d unitary
           representation matrix U
    Output: sequences Ans of SU(2) operations
      initialize Ans, set empty;
      for j ← 1 to d − 1 do
        if not U[d − j, d] = 0 then
          calculate an SU(2) operation u′ according to U[d, d]
          and U[d − j, d];
          add answer Ans ← Ans ∪ u′;
          update U ← u′U;
        end
      end
      add a generalized phase gate Ans ← Ans ∪ p making
      U[d, d] equal to 1;
      if d > 1 then
        return Ans ∪ GED(d − 1, U[1 : d − 1, 1 : d − 1]);
      else
        return Ans;
    end
```

The strategy of Gaussian elimination affects the implementation of sequences, and the normal and the bubbling ones are described in Algorithms 1 and 2, respectively. Although both of them provide no more than $d(d-1)/2$ SU(2) operations, the level structure of each SU(2) operation finally affects the pulse number required in the SU(d) operation. Obviously, the normal Gaussian elimination is more suitable for the trapped-ion system in Ref. [3], while the bubbling one is more suitable for the qudit in this work, which is close to the theoretical limit.

APPENDIX C: QUDIT PARAMETERS AND EXPERIMENTAL SETUP

Our qudit system is implemented on a transmon regarded as a multilevel system instead of the nominal two-level qubit. The fabrication of our device follows the same procedure as described in Ref. [68]. Table II shows its control and coherence parameters. $\omega_{m,n}/2\pi$ denotes the transition frequency between levels $|m\rangle$ and $|n\rangle$, and $T_1^{|m\rangle}$ indicates the characteristic time of energy relaxation if the qudit is initialized in the $|m\rangle$ state. $T_{2,\mathrm{Ramsey}}^{|m\rangle,|n\rangle}$ denotes the dephasing time measured via Ramsey interferometry protocol between levels $|m\rangle$ and $|n\rangle$. Higher levels are influenced more than lower ones by charge parity, causing fitting of the experimental data to be more difficult; a rough estimate of dephasing is therefore given for higher levels. Figure 8 shows the results of time-dependent Rabi oscillations under single- or two-photon transition without readout correction or phase correction. It is obvious that the transitions between adjacent levels are faster than the nonadjacent ones. Therefore, single-photon transitions are chosen as basic transitions to achieve high-fidelity manipulations.

The qudit device is installed in a dilution refrigerator with details shown in Fig. 9. Two microwave lines coupled to the Josephson junction and readout resonator are used to drive and detect. Readout signals are generated from the arbitrary wave generator and up-converted to 7.217 GHz to probe the four levels simultaneously at room temperature. Table III and Fig. 10(a) present the readout response parameters. A statistical analysis of the readout signal is shown in Fig. 10(b). We prepare the state $|k\rangle$ and calculate the standard deviation of acquiring the measurement result $|k\rangle$ as a function of repeated runs r by bootstrapping. The standard deviation of the experimental results decreases as r increases, reaching the theoretical convergence rate $1/\sqrt{r}$. An instance of the readout fidelity matrix is shown in Table IV.

The drive signal is generated from the same arbitrary wave generator but in a different channel. Different from the readout waveform, more frequency component waves are required for qudit manipulations. Furthermore, pulses of different frequencies are combined in the same drive pulse sequence. Phase differences between these pulses are important so that a common channel of an arbitrary waveform generator is employed. The pulse sequence is generated and up-converted to the frequencies we want via an in-phase and quadrature mixer at a local frequency of 4.8 GHz. We use $\pi/2$ cosine pulses with an arbitrary phase as basic components, whose duration between $|0\rangle$ and $|1\rangle$ ($|1\rangle$ and $|2\rangle$, $|2\rangle$ and $|3\rangle$) is 45 ns (35, 85 ns) with a 10-ns buffer.

TABLE II. Control and coherent parameters of the qudit device.

Adjacent one-photon transition frequency	(GHz)	Two-photon transition frequency	(GHz)	Lifetime of excited levels	(μs)	Dephasing time between labeled states	(μs)
$\omega_{01}/2\pi$	5.355	$\omega_{02}/2\pi$	5.241	$T_1^{\|1\rangle}$	180 ± 3	$T_{2,\mathrm{Ramsey}}^{\|0\rangle,\|1\rangle}$	76 ± 2
$\omega_{12}/2\pi$	5.127	$\omega_{13}/2\pi$	5.000	$T_1^{\|2\rangle}$	101 ± 1	$T_{2,\mathrm{Ramsey}}^{\|1\rangle,\|2\rangle}$	37 ± 3
$\omega_{23}/2\pi$	4.873	$\bar{\omega}_{24}/2\pi$[a]	4.727	$T_1^{\|3\rangle}$	73 ± 1	$T_{2,\mathrm{Ramsey}}^{\|2\rangle,\|3\rangle}$	22.8 ± 0.3
$\bar{\omega}_{34}/2\pi$[a]	4.581					$T_{2,\mathrm{Ramsey}}^{\|3\rangle,\|4\rangle}$	≥ 10

[a]Average transition frequency between the corresponding levels.

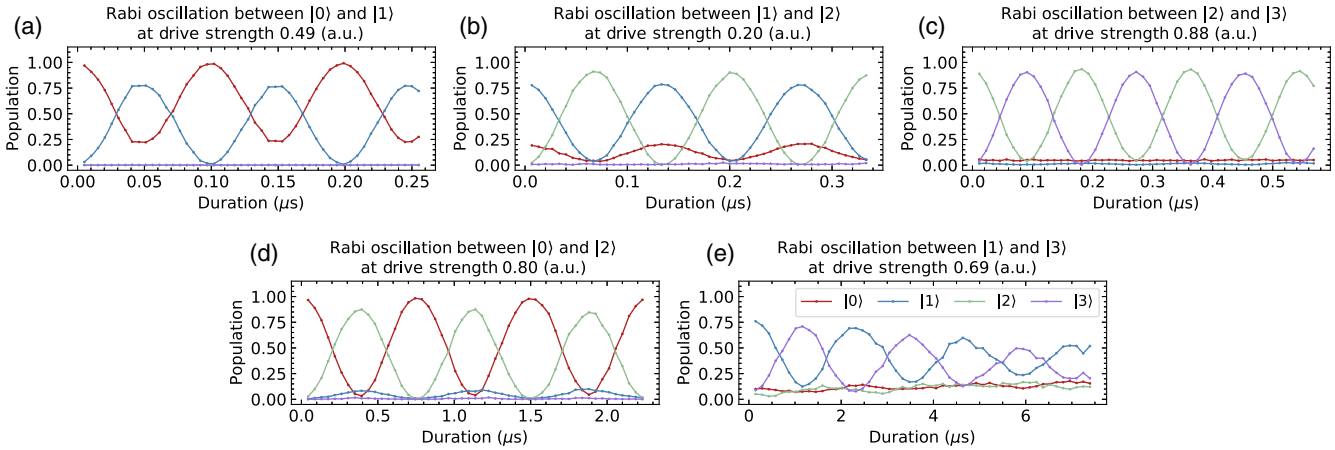

FIG. 8. Basic microwave-driven transitions in the transmon qudit. Transitions between adjacent levels are shown in (a)–(c) without readout correction or phase correction. Two-photon transitions are also observed and displayed in (d) and (e). The population damping in (e) is due to the frequency dichotomy of the higher level, and the signal is within the first period of the oscillation beat.

To calibrate the $\pi/2$ pulse, we determine the drive frequency using Ramsey interferometry. If interference with a beat is found in the Ramsey signal, the mean of the two frequencies is taken. Then we determine the frequency shift according to the derivative reduction by adiabatic gate [69] method for phase error. In fact, this dichotomy of the transition frequency influences our manipulation capability and makes the phase error difficult to calibrate. The amplitude of the pulse will be influenced at a nonzero frequency shift, so the above two steps are repeated for more precise calibration. Figures 11(a)–11(c) show randomized benchmarking sequences on SU(2) subspace $|0\rangle$ and $|1\rangle$, $|1\rangle$ and $|2\rangle$, and $|2\rangle$ and $|3\rangle$, respectively, with a fidelity $(99.979 \pm 0.001)\%$, $(99.924 \pm 0.004)\%$, and $(99.85 \pm 0.01)\%$ per $\pi/2$ pulse. Rather than having the subspaces spanned by adjacent levels, randomized benchmarking sequences are also applied via composite rotations from SU(2) transitions. Figure 11(e) shows that the fidelities of the $\pi/2$ pulses between $|0\rangle$ and $|2\rangle$, $|1\rangle$ and $|3\rangle$, and $|0\rangle$ and $|3\rangle$ are, respectively, $(99.49 \pm 0.01)\%$, $(99.55 \pm 0.02)\%$, and $(99.14 \pm 0.01)\%$. As measurements on the four levels are implemented simultaneously, leakages induced by

Algorithm 2. Bubbling Gaussian elimination decomposition of SU(d).

Function GED(d, U)**:**
  Input: current dimension d and the $d \times d$ unitary representation matrix U
  Output: sequences *Ans* of SU(2) operations spanned only on adjacent levels
  initialize *Ans*, set empty;
  for $j \leftarrow 1$ **to** $d-1$ **do**
    if *not* $U[j,d] = 0$ **then**
      calculate an SU(2) operation u' according to $U[j+1,d]$ and $U[j,d]$;
      add answer $Ans \leftarrow Ans \cup u'$;
      update $U \leftarrow u'U$;
    end
  end
  add a generalized phase gate $Ans \leftarrow Ans \cup p$ making $U[d,d]$ equal to 1;
  if $d > 1$ **then**
    return $Ans \cup$ GED$(d-1, U[1:d-1, 1:d-1])$;
  else
    return *Ans*;
  end

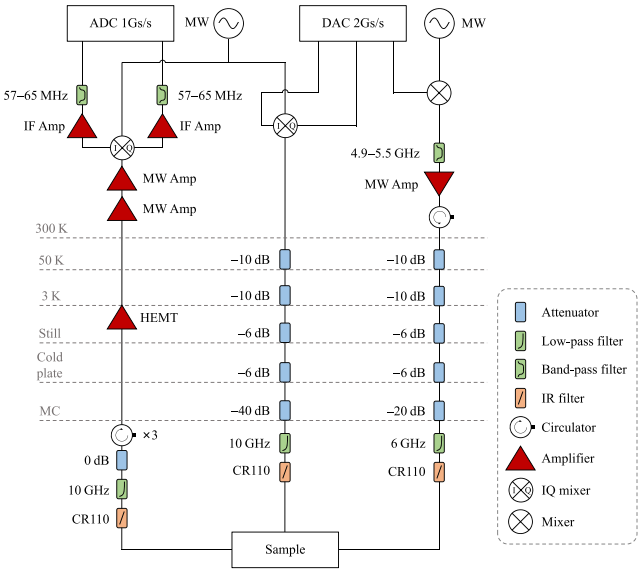

FIG. 9. A schematic of the measurement system includes the cryogenic and room-temperature setup. Digital-to-analog converter (DAC) is the arbitrary waveform generator, while analog-to-digital converter (ADC) is the waveform collector. Two microwave generators (MW) are employed to generate local signals.

TABLE III. Readout parameters of the qudit device.

Cavity response frequency for different qudit state $\|k\rangle$	(GHz)	Half high and half wide	(MHz)	Other parameters	Value
$\omega_{\|0\rangle}/2\pi$	7.217 85	$\gamma_{\|0\rangle}/2\pi$	0.22	Selected readout frequency $\omega_r/2\pi$	7.217 26 GHz
$\omega_{\|1\rangle}/2\pi$	7.217 48	$\gamma_{\|1\rangle}/2\pi$	0.23	Dispersive shift $\chi/2\pi$	0.34 MHz
$\omega_{\|2\rangle}/2\pi$	7.217 17	$\gamma_{\|2\rangle}/2\pi$	0.28	Readout coupling strength $g/2\pi$	76 MHz
$\omega_{\|3\rangle}/2\pi$	7.216 83	$\gamma_{\|3\rangle}/2\pi$	0.27		

energy relaxation or frequency bandwidth contribute to incoherent errors for SU(2) manipulations, which may not be observed directly by RB in two-level systems. Derivative reduction by an adiabatic gate is usually adopted to suppress unwanted frequency components with driving pulses in qubit manipulations [69]. Inspired by the above, a similar approach could be used to suppress unwanted frequency components in qudit manipulation. However,

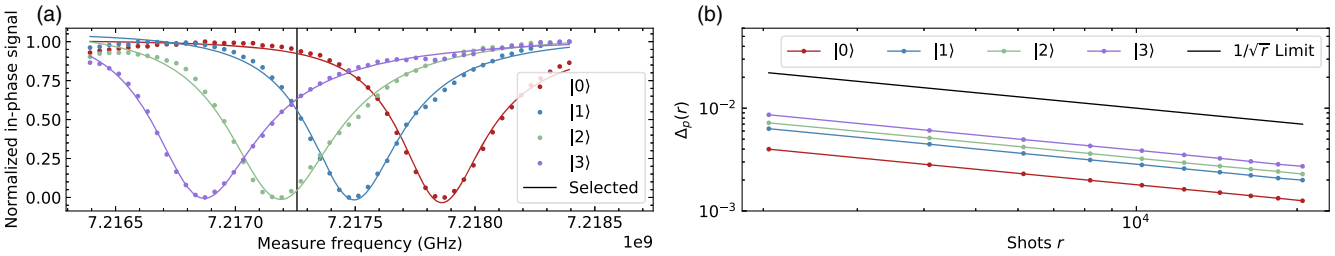

FIG. 10. (a) In-phase response signal at changing measurement frequency. The cavity responds differently when the qubit is prepared in a different state $|k\rangle$. The black solid line indicates the frequency we select for state discrimination. (b) Standard deviation for state discrimination calculated by bootstrapping. From a total of 20480 runs of $|k\rangle$ state measurements, r runs are randomly chosen to calculate the standard deviation $\Delta_p(r)$ with $p = 1$ when a run gives the measurement $|k\rangle$ and otherwise $p = 0$, and this process is averaged over 50 000 repetitions and provides $\Delta_p(r)$ as a function of r plotted in chosen colors for different initial states. The expected convergence limit $1/\sqrt{r}$ is given by the black solid line.

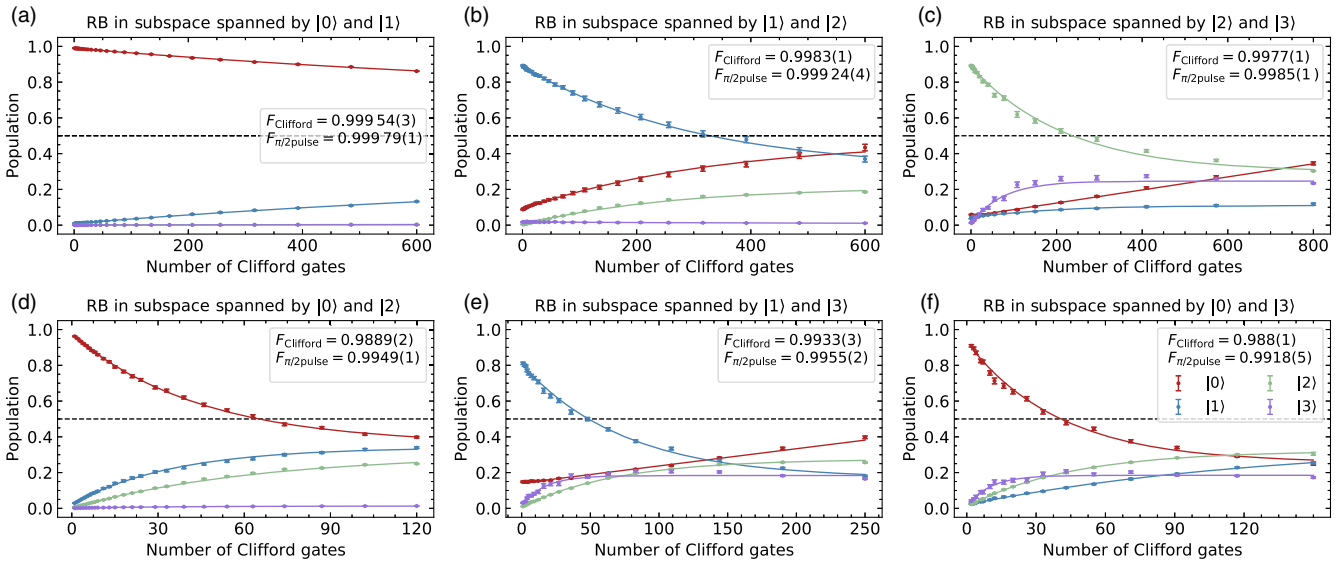

FIG. 11. Randomized benchmarking on arbitrary SU(2) subspace. Note that in (a) $|0\rangle$ and $|1\rangle$, (b) $|1\rangle$ and $|2\rangle$, (c) $|2\rangle$ and $|3\rangle$, only adjacent transitions are used in the corresponding subspace after initial-state preparation with slightly different RB sequences, requiring different average $\pi/2$ pulses per Clifford gate, numbered 2.167, 2.167, and 1.5, respectively. (d) $|0\rangle$ and $|2\rangle$, (e) $|1\rangle$ and $|3\rangle$, (f) $|0\rangle$ and $|3\rangle$ focus on operations over the corresponding subspaces and therefore are combinations of adjacent transitions. All four states are measured, and the results are plotted as crosses with error bars and full line fitting in corresponding colors. Black dotted lines indicate the population of a mixed state of SU(2) after evolving for a sufficiently long time.

TABLE IV. An instance of preparation and readout fidelity.

	Detect $\|0\rangle$	Detect $\|1\rangle$	Detect $\|2\rangle$	Detect $\|3\rangle$
Prepare $\|0\rangle$	0.991 04	0.008 31	0.000 60	0.000 05
Prepare $\|1\rangle$	0.053 53	0.944 59	0.000 71	0.001 17
Prepare $\|2\rangle$	0.024 28	0.029 95	0.944 98	0.000 79
Prepare $\|3\rangle$	0.037 80	0.006 89	0.044 19	0.911 12

the driving scheme would become more involved, because there are now more frequency components to suppress.

Unfortunately, randomized benchmarking cannot estimate all error messages, due to the averaging effect of the RB sequence. Some specific types of errors, such as the non-Markovian error in operation, cannot be observed, and only limited manipulation errors can be perceived. In qubit systems, such errors can be estimated by gate set tomography [54,55]. However, for a qudit system, related theoretical tools are still being developed or discovered. It calls for increased theoretical efforts, as analyzing the error source is of great importance to improve manipulation.

APPENDIX D: QUANTUM-STATE TOMOGRAPHY OF THE QUDIT

QST is a common method to determine the density matrix of a quantum state. QST of a qudit system was presented in a nuclear-magnetic-resonance system [46], and we follow the same method. To measure elements of an arbitrary density matrix of a qudit, for example, a four-level system, we construct 12 operations $\hat{M}_l, l = 0, 1, \ldots, 11$, as in the following:

$$\begin{aligned}
\hat{M}_0 &= \hat{R}_{0,1}\left(-\frac{\pi}{2}, 0\right),\\
\hat{M}_1 &= \hat{R}_{1,2}\left(-\frac{\pi}{2}, 0\right),\\
\hat{M}_2 &= \hat{R}_{2,3}\left(-\frac{\pi}{2}, 0\right),\\
\hat{M}_3 &= \hat{R}_{0,1}\left(-\frac{\pi}{2}, \frac{\pi}{2}\right),\\
\hat{M}_4 &= \hat{R}_{1,2}\left(-\frac{\pi}{2}, \frac{\pi}{2}\right),\\
\hat{M}_5 &= \hat{R}_{2,3}\left(-\frac{\pi}{2}, \frac{\pi}{2}\right),\\
\hat{M}_6 &= \hat{R}_{1,2}\left(-\frac{\pi}{2}, 0\right)\hat{R}_{0,1}\left(-\frac{\pi}{2}, 0\right),\\
\hat{M}_7 &= \hat{R}_{1,2}\left(-\frac{\pi}{2}, \frac{\pi}{2}\right)\hat{R}_{0,1}\left(-\frac{\pi}{2}, 0\right),\\
\hat{M}_8 &= \hat{R}_{2,3}\left(-\frac{\pi}{2}, 0\right)\hat{R}_{1,2}\left(-\frac{\pi}{2}, 0\right),\\
\hat{M}_9 &= \hat{R}_{2,3}\left(-\frac{\pi}{2}, \frac{\pi}{2}\right)\hat{R}_{1,2}\left(-\frac{\pi}{2}, 0\right),\\
\hat{M}_{10} &= \hat{R}_{2,3}\left(-\frac{\pi}{2}, \frac{\pi}{2}\right)\hat{R}_{1,2}\left(-\frac{\pi}{2}, \frac{\pi}{2}\right)\hat{R}_{0,1}\left(-\frac{\pi}{2}, \frac{\pi}{2}\right),\\
\hat{M}_{11} &= \hat{R}_{2,3}\left(-\frac{\pi}{2}, 0\right)\hat{R}_{1,2}\left(-\frac{\pi}{2}, 0\right)\hat{R}_{1,2}\left(-\frac{\pi}{2}, 0\right). \qquad \text{(D1)}
\end{aligned}$$

For an unknown quantum state $\hat{\rho}$, we apply each operation after state preparation, followed by a measurement gate which projects the state into one of the four eigenstates $|0\rangle$, $|1\rangle$, $|2\rangle$, and $|3\rangle$, and the respective probabilities $P_{l,k} = \langle k|\hat{M}_l^\dagger \hat{\rho} \hat{M}_l|k\rangle$ with $l = 0, 1, \ldots, 11$ and $k = 0, 1, 2, 3$ are obtained, satisfying $\sum_k P_{l,k} = 1$. Elements of $\hat{\rho}$ are solved according to

$$\begin{aligned}
\rho_{0,0} &= (P_{2,0} + P_{5,0})/2,\\
\rho_{1,1} &= (P_{2,1} + P_{5,2})/2,\\
\rho_{2,2} &= (P_{0,2} + P_{0,3})/2,\\
\rho_{3,3} &= (P_{0,3} + P_{3,3})/2,\\
x_{0,1} &= (P_{3,0} - P_{3,1})/2,\\
x_{1,2} &= (P_{4,1} - P_{4,2})/2,\\
x_{2,3} &= (P_{5,2} - P_{5,3})/2,\\
y_{0,1} &= (P_{0,0} - P_{0,1})/2,\\
y_{1,2} &= (P_{1,1} - P_{1,2})/2,\\
y_{2,3} &= (P_{2,2} - P_{2,3})/2,\\
x_{0,2} &= (P_{6,1} - P_{6,2} - \sqrt{2}y_{1,2})/\sqrt{2},\\
y_{0,2} &= (P_{7,2} - P_{7,1} + \sqrt{2}x_{1,2})/\sqrt{2},\\
x_{1,3} &= (P_{8,2} - P_{8,3} - \sqrt{2}y_{2,3})/\sqrt{2},\\
y_{1,3} &= (P_{9,3} - P_{9,2} + \sqrt{2}x_{2,3})/\sqrt{2},\\
x_{0,3} &= P_{10,2} - P_{10,3} - \sqrt{2}x_{2,3} + x_{1,3},\\
y_{0,3} &= P_{11,3} - P_{11,2} + \sqrt{2}y_{2,3} + x_{1,3},\\
\rho_{0,1} &= x_{0,1} + iy_{0,1},\\
\rho_{0,2} &= x_{0,2} + iy_{0,2},\\
\rho_{0,3} &= x_{0,3} + iy_{0,3},\\
\rho_{1,2} &= x_{1,2} + iy_{0,2},\\
\rho_{1,3} &= x_{1,3} + iy_{0,3},\\
\rho_{2,3} &= x_{2,3} + iy_{0,3}. \qquad \text{(D2)}
\end{aligned}$$

Unfortunately, the state obtained this way does not make full use of the information in the measurement data. An alternative method is to apply MLE according to the properties of the density matrix [51,52], with the simple estimation $\hat{\rho}$ from Eq. (D2) regarded as an initial guess to

reduce the impact of other undesirable errors on the output density matrix.

APPENDIX E: QUANTUM-PROCESS TOMOGRAPHY OF A QUDIT

QPT is based on quantum-state tomography [3] providing a convenient visible method to characterize a quantum process. Like QPT of a qubit, we initialize our d-level system in a given state, then apply the process we want to determine, and end with QST to measure the final state. In Ref. [49], for arbitrary state $|m\rangle\langle n|$, which is obviously the basis of the density matrix, the final state after the process $\mathcal{E}(|m\rangle\langle n|)$ satisfies

$$\mathcal{E}(|m\rangle\langle n|) = \mathcal{E}(|+\rangle\langle +|) + i\mathcal{E}(|-\rangle\langle -|) - \frac{1+i}{2}\mathcal{E}(|m\rangle\langle m|) - \frac{1+i}{2}\mathcal{E}(|n\rangle\langle n|), \quad \text{(E1)}$$

where $|+\rangle = (|m\rangle + |n\rangle)/\sqrt{2}$ and $|-\rangle = (|m\rangle + i|n\rangle)/\sqrt{2}$, and the pure state $|n\rangle$, $|m\rangle$, $|+\rangle$, or $|-\rangle$ can be prepared from the initial state $|0\rangle$. Our implementation, however, tests another set of initial states

$$|a_m\rangle \equiv |m\rangle, \quad \text{(E2)}$$

$m = 0, 1, \ldots, d-1$, and

Algorithm 3. Construction of generators of the SU(d) matrix.

Input: order d of SU(d)
Output: sequences *Ans* of SU(d) generators in matrix representation

initialize *Ans*, set empty;
add answer $Ans \leftarrow Ans \cup \mathrm{I}_{d\times d}$;
for $j \leftarrow 2$ **to** d **do**
  for $k \leftarrow 0$ **to** $j-2$ **do**
    add answer $Ans \leftarrow Ans \cup \rho_{m,n} = \begin{cases} 1, & m = k, n = j-1, \\ 1, & m = j-1, n = k, ; \\ 0, & \text{otherwise}, \end{cases}$
    add answer $Ans \leftarrow Ans \cup \rho_{m,n} = \begin{cases} -i, & m = k, n = j-1, \\ i, & m = j-1, n = k, ; \\ 0, & \text{otherwise}, \end{cases}$
  end
  add answer $Ans \leftarrow Ans \cup \rho_{m,n} = \begin{cases} \frac{1}{\sqrt{j(j-1)/2}}, & m = n = 0, 1, \ldots, j-2, \\ \frac{1-j}{\sqrt{j(j-1)/2}}, & m = n = j-1; \\ 0, & \text{otherwise}, \end{cases}$
end
return *Ans*;

$$|a_{m,n,0}\rangle \equiv (|m\rangle - |n\rangle)/\sqrt{2},$$
$$|a_{m,n,1}\rangle \equiv (|m\rangle - i|n\rangle)/\sqrt{2},$$
$$|a_{m,n,2}\rangle \equiv (|m\rangle + i|n\rangle)/\sqrt{2}, \quad \text{(E3)}$$

for $m, n = 0, 1, \ldots, d-1$ and $m < n$. It is obvious that the first d items initialize the system via

$$\hat{a}_m = \hat{R}_{m-1,m}\left(\pi, \frac{\pi}{2}\right)\hat{R}_{m-2,m-1}\left(\pi, \frac{\pi}{2}\right)\cdots\hat{R}_{0,1}\left(\pi, \frac{\pi}{2}\right), \quad \text{(E4)}$$

with $\hat{a}_m|0\rangle = |a_m\rangle$, and therefore,

$$\hat{a}_{m,n,0} = \hat{R}_{m,n}\left(\frac{\pi}{2}, -\frac{\pi}{2}\right)\hat{a}_m,$$
$$\hat{a}_{m,n,1} = \hat{R}_{m,n}\left(\frac{\pi}{2}, 0\right)\hat{a}_m,$$
$$\hat{a}_{m,n,2} = \hat{R}_{m,n}\left(\frac{\pi}{2}, -\frac{\pi}{2}\right)\hat{a}_m, \quad \text{(E5)}$$

with $\hat{a}_{m,n,k}|0\rangle = |a_{m,n,k}\rangle$ for $k = 0, 1, 2$. A total of $d + 3d(d-1)/2 = d(3d-1)/2$ initial states are prepared accordingly. After the final states are measured with QST, we have

$$-\mathcal{E}(|m\rangle\langle n|) = \mathcal{E}(|a_{m,n,0}\rangle\langle a_{m,n,0}|) + i\mathcal{E}(|a_{m,n,1}\rangle\langle a_{m,n,1}|) - \frac{1+i}{2}\mathcal{E}(|m\rangle\langle m|) - \frac{1+i}{2}\mathcal{E}(|n\rangle\langle n|),$$
$$-\mathcal{E}(|n\rangle\langle m|) = \mathcal{E}(|a_{m,n,0}\rangle\langle a_{m,n,0}|) + i\mathcal{E}(|a_{m,n,2}\rangle\langle a_{m,n,2}|) - \frac{1+i}{2}\mathcal{E}(|m\rangle\langle m|) - \frac{1+i}{2}\mathcal{E}(|n\rangle\langle n|). \quad \text{(E6)}$$

If we regard state set $\{|0\rangle\langle 0|, |0\rangle\langle 1|, \ldots, |0\rangle\langle d-1|, |1\rangle\langle 0|, |1\rangle\langle 1|, \ldots, |1\rangle\langle d-1|, \ldots, |d-1\rangle\langle 0|, |d-1\rangle\langle 1|, \ldots, |d-1\rangle\langle d-1|\}$ as a group of basis, a superoperator representation can be recovered from $\mathcal{E}(|m\rangle\langle n|)$ labeled by $\hat{\chi}_0$ whose matrix representation is of dimension $d^2 \times d^2$. In this work, an alternative group of basis to represent the superoperator is taken, leading to satisfactory matrix representation of the superoperator. We choose the identity matrix of order d, $d^2 - 1$ generators of the SU(d) matrix, and sequence $\lambda_0, \lambda_1, \ldots, \lambda_{d^2-1}$ which are obtained from Algorithm 3, as our basis $\{\hat{\lambda}_k\}$ to represent the superoperator. The relationship

$$\hat{\rho} = \sum_{k,l}\hat{\lambda}_k\hat{\rho}\hat{\lambda}_l^{\dagger}\chi_{k,l}, \quad \text{(E7)}$$

with $\hat{\rho}$ an arbitrary density operator of the system, describes the calculation of $\hat{\chi}$, and the results are shown in Figs. 5(b) and 5(c) for $d = 3$ and $d = 4$.

The MLE can also be adapted to QPT. One can choose to use the MLE in QST for each step to aim for a more precise state-tomography result, or directly using it in the whole

calculation according to the properties of the matrix representation of the superoperator under the special basis chosen here. A positive-semidefinite matrix allows us to choose the MLE.

For $d = 3$,

$$\lambda_0 = \begin{pmatrix} 1 & 0 & 0 \\ 0 & 1 & 0 \\ 0 & 0 & 1 \end{pmatrix}, \quad \lambda_1 = \begin{pmatrix} 0 & 1 & 0 \\ 1 & 0 & 0 \\ 0 & 0 & 0 \end{pmatrix},$$
$$\lambda_2 = \begin{pmatrix} 0 & -i & 0 \\ i & 0 & 0 \\ 0 & 0 & 0 \end{pmatrix}, \quad \lambda_3 = \begin{pmatrix} 1 & 0 & 0 \\ 0 & -1 & 0 \\ 0 & 0 & 0 \end{pmatrix},$$
$$\lambda_4 = \begin{pmatrix} 0 & 0 & 1 \\ 0 & 0 & 0 \\ 1 & 0 & 0 \end{pmatrix}, \quad \lambda_5 = \begin{pmatrix} 0 & 0 & -i \\ 0 & 0 & 0 \\ i & 0 & 0 \end{pmatrix},$$
$$\lambda_6 = \begin{pmatrix} 0 & 0 & 0 \\ 0 & 0 & 1 \\ 0 & 1 & 0 \end{pmatrix}, \quad \lambda_7 = \begin{pmatrix} 0 & 0 & 0 \\ 0 & 0 & -i \\ 0 & i & 0 \end{pmatrix},$$
$$\lambda_8 = \frac{1}{\sqrt{3}} \begin{pmatrix} 1 & 0 & 0 \\ 0 & 1 & 0 \\ 0 & 0 & -2 \end{pmatrix}, \tag{E8}$$

and for $d = 4$,

$$\lambda_0 = \begin{pmatrix} 1 & 0 & 0 & 0 \\ 0 & 1 & 0 & 0 \\ 0 & 0 & 1 & 0 \\ 0 & 0 & 0 & 1 \end{pmatrix}, \quad \lambda_1 = \begin{pmatrix} 0 & 1 & 0 & 0 \\ 1 & 0 & 0 & 0 \\ 0 & 0 & 0 & 0 \\ 0 & 0 & 0 & 0 \end{pmatrix},$$
$$\lambda_2 = \begin{pmatrix} 0 & -i & 0 & 0 \\ i & 0 & 0 & 0 \\ 0 & 0 & 0 & 0 \\ 0 & 0 & 0 & 0 \end{pmatrix}, \quad \lambda_3 = \begin{pmatrix} 1 & 0 & 0 & 0 \\ 0 & -1 & 0 & 0 \\ 0 & 0 & 0 & 0 \\ 0 & 0 & 0 & 0 \end{pmatrix},$$
$$\lambda_4 = \begin{pmatrix} 0 & 0 & 1 & 0 \\ 0 & 0 & 0 & 0 \\ 1 & 0 & 0 & 0 \\ 0 & 0 & 0 & 0 \end{pmatrix}, \quad \lambda_5 = \begin{pmatrix} 0 & 0 & -i & 0 \\ 0 & 0 & 0 & 0 \\ i & 0 & 0 & 0 \\ 0 & 0 & 0 & 0 \end{pmatrix},$$
$$\lambda_6 = \begin{pmatrix} 0 & 0 & 0 & 0 \\ 0 & 0 & 1 & 0 \\ 0 & 1 & 0 & 0 \\ 0 & 0 & 0 & 0 \end{pmatrix}, \quad \lambda_7 = \begin{pmatrix} 0 & 0 & 0 & 0 \\ 0 & 0 & -i & 0 \\ 0 & i & 0 & 0 \\ 0 & 0 & 0 & 0 \end{pmatrix},$$
$$\lambda_8 = \frac{1}{\sqrt{3}} \begin{pmatrix} 1 & 0 & 0 & 0 \\ 0 & 1 & 0 & 0 \\ 0 & 0 & -2 & 0 \\ 0 & 0 & 0 & 0 \end{pmatrix}, \quad \lambda_9 = \begin{pmatrix} 0 & 0 & 0 & 1 \\ 0 & 0 & 0 & 0 \\ 0 & 0 & 0 & 0 \\ 1 & 0 & 0 & 0 \end{pmatrix},$$
$$\lambda_{10} = \begin{pmatrix} 0 & 0 & 0 & -i \\ 0 & 0 & 0 & 0 \\ 0 & 0 & 0 & 0 \\ i & 0 & 0 & 0 \end{pmatrix}, \quad \lambda_{11} = \begin{pmatrix} 0 & 0 & 0 & 0 \\ 0 & 0 & 0 & 1 \\ 0 & 0 & 0 & 0 \\ 0 & 1 & 0 & 0 \end{pmatrix},$$
$$\lambda_{12} = \begin{pmatrix} 0 & 0 & 0 & 0 \\ 0 & 0 & 0 & -i \\ 0 & 0 & 0 & 0 \\ 0 & i & 0 & 0 \end{pmatrix}, \quad \lambda_{13} = \begin{pmatrix} 0 & 0 & 0 & 0 \\ 0 & 0 & 0 & 0 \\ 0 & 0 & 0 & 1 \\ 0 & 0 & 1 & 0 \end{pmatrix},$$
$$\lambda_{14} = \begin{pmatrix} 0 & 0 & 0 & 0 \\ 0 & 0 & 0 & 0 \\ 0 & 0 & 0 & -i \\ 0 & 0 & i & 0 \end{pmatrix}, \quad \lambda_{15} = \frac{1}{\sqrt{6}} \begin{pmatrix} 1 & 0 & 0 & 0 \\ 0 & 1 & 0 & 0 \\ 0 & 0 & 1 & 0 \\ 0 & 0 & 0 & -3 \end{pmatrix}. \tag{E9}$$

APPENDIX F: CONSTRUCTION OF SU(3) AND SU(4) CLIFFORD OPERATIONS

For the Clifford group $\boldsymbol{C}_d^n$ and Pauli group $\boldsymbol{P}_d^n$, where d is the qudit Hilbert-space dimension and n is the number of qudits, the quotient group $\boldsymbol{C}_d^n/\boldsymbol{P}_d^n$ is isomorphic to the symplectic group $\mathrm{Sp}(dn)$. The number of the Clifford group elements can be calculated by $N_{P_d^n} \times N_{\mathrm{Sp}(dn)}$ for arbitrary $\boldsymbol{C}_d^n$. We can generate a single-qudit Clifford group with the

Algorithm 4. Construction of SU(d) Clifford operations.

```
Function Clifford(n = 1, d):
    Input: qudit number n default to 1 and qudit dimension d
    Output: Clifford group for SU(d)
    initialize N_SU(d) ← N_{P_d^n} × N_Sp(d);
    initialize set Group ← [F_d, S_d, Z_d, X_d];
    initialize h ← 0, j ← 0, L ← len(Group);
    while h < L do
        for k ← j to L do
            g ← Group[h] * Group[k];
            Group ← Group ∪ g, a global complex factor allowed;
            g ← Group[k] * Group[h];
            Group ← Group ∪ g, a global complex factor allowed;
        end
        if len(Group) = N_SU(d) then
            return Group;
        end
        if len(Group) = L then
            h ← h + 1;
            j ← 0;
        else
            j ← L;
            L ← len(Group);
        end
    end
```

generators F_d, P_d, Z_d, and X_d. With the orthonormal computational basis $|s\rangle; s \in \mathbb{Z}_d$, $\mathbb{Z}_d \coloneqq 0, 1, \ldots, d-1$, $F_d|s\rangle \coloneqq (1/\sqrt{d}) \sum_{s' \in \mathbb{Z}_d} \omega^{ss'} |s'\rangle$ which is the quantum Fourier transform, and the phase gate $P|s\rangle \coloneqq \omega^{\frac{s(s+\rho_d)}{2}}|s\rangle$, with $\rho_d = 1$ for odd d and $\rho_d = 0$ otherwise, to obtain $X_d|s\rangle = |s \oplus 1\rangle$ and $Z_d|s\rangle = \omega^s|s\rangle$, where $\omega \coloneqq \exp(2\pi i/d)$. To construct Clifford group operations for SU(d), we follow Algorithm 4.

APPENDIX G: DETAILS FOR CYCLIC PERMUTATION PARITY CHECK

1. Parity check of cyclic permutation

One application of DFT is to check the parity of cyclic permutation. In this algorithm, for a permutation of length d we want to check if the qudit is initialized into a coherent superposition state DFT$|m\rangle$, and then permutation operation $\hat{U}_k, k = 1, 2, \ldots, d!$ is applied. Before reading out the qudit, an inverse DFT labeled by DFT^{-1} is applied to transform the state. Different outcomes from the readout reveal parities of cyclic permutations. We remind that the choice of the initial state affects the result of the algorithm with $m = 0$, the trivial case, and can be neglected, and m and d are coprime numbers, i.e., $\gcd(m, d) = 1$. Parities of cyclic permutations can be directly measured from populations of $|m\rangle$ and $|d-m\rangle$, with the former for even parity and the latter for odd parity. If other initial states are chosen, the results would be more complicated, but they remain completely determined. For example, taking $\gcd(m, d) = t$, then $d = qt$, the subgroup $\mathcal{G}(m, d) = \langle \hat{Q} \rangle$ of permutations of length d satisfies

$$\hat{Q} = \begin{bmatrix} j & (j+q) \bmod d \\ (j+q) \bmod d & j \end{bmatrix}, \quad \text{(G1)}$$

$j = 0, 1, \ldots, d-1$. If the readout of $\hat{U}_k$ is still $|m\rangle$, $\hat{U}_k \in g\mathcal{C}_{d,\text{even}}$, $\forall\ g \in \mathcal{G}(m, d)$, where $C_{d,\text{even}}$ is the set of d-length cyclic permutation of even parity, whereas if the readout gives $|d-m\rangle$, $\hat{U}_k \in g\mathcal{C}_{d,\text{odd}}$, $\forall\ g \in \mathcal{G}(m, d)$. Obviously, $t = 1$ corresponds to the trivial case where $\mathcal{G}(m, d)$ is the identity group.

For permutations of length-3, $\gcd(2, 3) = 1$, we know the parity from $|2\rangle$ or $|1\rangle$ readout at the end of a circuit. The cyclic operations are from

$$\hat{U}_1 = \begin{bmatrix} 0 & 1 & 2 \\ 0 & 1 & 2 \end{bmatrix}, \quad \hat{U}_4 = \begin{bmatrix} 0 & 1 & 2 \\ 1 & 2 & 0 \end{bmatrix}, \quad \hat{U}_5 = \begin{bmatrix} 0 & 1 & 2 \\ 2 & 0 & 1 \end{bmatrix}, \quad \text{(G2)}$$

and implicate even parity for final state $|2\rangle$, while

$$\hat{U}_2 = \begin{bmatrix} 0 & 1 & 2 \\ 0 & 2 & 1 \end{bmatrix}, \quad \hat{U}_3 = \begin{bmatrix} 0 & 1 & 2 \\ 1 & 0 & 2 \end{bmatrix}, \quad \hat{U}_6 = \begin{bmatrix} 0 & 1 & 2 \\ 2 & 1 & 0 \end{bmatrix} \quad \text{(G3)}$$

give odd parity for final state $|1\rangle$. However, for permutations of length-4, a special case satisfying $N = 2m$, both parities give the same readout and

$$\bigcup_{g \in \mathcal{G}(2,4)} gC(4) = C(4), \quad \text{(G4)}$$

where $C(4)$ is the set of all length-4 cyclic permutations and $|C(4)| = 8$. In other words, the parity check of length-4 cyclic permutations is invalid, but cyclic permutations can still be distinguished with

$$\begin{aligned} \hat{U}_1 &= \begin{bmatrix} 0 & 1 & 2 & 3 \\ 0 & 1 & 2 & 3 \end{bmatrix}, & \hat{U}_6 &= \begin{bmatrix} 0 & 1 & 2 & 3 \\ 0 & 3 & 2 & 1 \end{bmatrix}, \\ \hat{U}_8 &= \begin{bmatrix} 0 & 1 & 2 & 3 \\ 1 & 0 & 3 & 2 \end{bmatrix}, & \hat{U}_{10} &= \begin{bmatrix} 0 & 1 & 2 & 3 \\ 1 & 2 & 3 & 0 \end{bmatrix}, \\ \hat{U}_{15} &= \begin{bmatrix} 0 & 1 & 2 & 3 \\ 2 & 1 & 0 & 3 \end{bmatrix}, & \hat{U}_{17} &= \begin{bmatrix} 0 & 1 & 2 & 3 \\ 2 & 3 & 0 & 1 \end{bmatrix}, \\ \hat{U}_{19} &= \begin{bmatrix} 0 & 1 & 2 & 3 \\ 3 & 0 & 1 & 2 \end{bmatrix}, & \hat{U}_{24} &= \begin{bmatrix} 0 & 1 & 2 & 3 \\ 3 & 2 & 1 & 0 \end{bmatrix} \end{aligned} \quad \text{(G5)}$$

from experiment results.

2. The simplest construction of permutation operations

In order to construct $\hat{U}_k$ using pulses as short as possible, some considerations can help to simplify the pulse sequence of $\hat{U}_k$ according to the nature of the permutation and commutation inspired by the bubble sort algorithm from Ref. [70]. For a permutation $\hat{U}_k$ of length d,

$$\hat{U}_k = \begin{bmatrix} 0 & 1 & \cdots & N-1 \\ p_{k,0} & p_{k,1} & \cdots & p_{k,d-1} \end{bmatrix} \quad \text{(G6)}$$

satisfying $\hat{U}_k|j\rangle = |p_{k,j}\rangle$, where $p_{k,j} \in \{0, 1, \ldots, d-1\}$, $\forall\ j \in \{0, 1, \ldots, d-1\}$, and $\forall\ j_1 \neq j_2, p_{k,j_1} \neq p_{k,j_2}$, and k indicate the ascending lexicographical order of $p_{k,1}, p_{k,2}, \ldots, p_{k,d}$. Therefore, each $\hat{U}_k$ takes its matrix representation $\mathbf{M}(\hat{U}_k)$, and it is easy to prove that $\hat{U}_k$ is unitary. While normal Gaussian elimination is certainly a universal method to translate matrix representations into pulse sequences, it is a bit awkward in this situation, with each permutation equivalent to the product of several transpositions. The basic pulse $\hat{R}_{j,j+1}(\theta, \phi)$ we employ actually corresponds to transitions between adjacent levels, and using only adjacent transpositions can construct arbitrary permutations, and finding minimum numbers of adjacent transpositions is of great importance to pulse sequence simplification. A transposition between adjacent levels can be written as $\hat{X}_{j,j+1} = |j+1\rangle\langle j| + |j\rangle\langle j+1|$.

A simple perspective to understand the lower bound of the adjacent transposition numbers comes from the

Algorithm 5. Bubble construction of $\hat{U}_k$.

Input: an array $\{p_{k,j}\}, j = 0, 1, \ldots, d-1$ representing U_k to be constructed
Output: sequences *Ans* of SU(2) operations in adjacent levels

```
initialize Ans, set empty;
while True do
    initialize flag f ← True;
    for j ← 0 to d − 2 do
        if p_{k,j} > p_{k,j+1} then
            swap p_{k,j} and p_{k,j+1};
            add an adjacent transposition
             Ans ← Ans ∪ X̂_{j,j+1};
            update flag f ← False;
        end
    end
    if f then
        return Ans;
    end
end
```

inversion pairs of a permutation. For a given permutation, inversion pairs are determined, and an adjacent transposition would increase or decrease an inversion. The number of adjacent transpositions is no less than the inverse pairs in a permutation. If a sequence with a number of adjacent transpositions equals the inverse pairs, the minimal decomposition is found.

We can use bubbling Gaussian elimination to generate the pulse sequence of $\hat{U}_k$, with the same results obtained. Hopefully, this helps us understand why the bubbling elimination corresponds to the limit of theoretical complexity of the transmon qudit.

APPENDIX H: VQE IN A QUDIT

1. Framework of VQE

For a molecule consisting of N nuclei and M (valence) electrons free from external field, its electronic Hamiltonian [71] is expressed in K canonical molecular orbitals as

$$\hat{H}_0 = \sum_{p,q=1}^{K} h_{pq} a_p^\dagger a_q + \frac{1}{2} \sum_{p,q,r,s=1}^{K} h_{pqrs} a_p^\dagger a_q^\dagger a_s a_r, \quad \text{(H1)}$$

where p, q, r, and s denote different spin orbitals and parameters (one-electron h_{pq} and two-electron h_{pqrs} integrals), and

$$h_{pq} = \int d\mathbf{x} \phi_p^*(\mathbf{x}) \left(-\frac{\nabla^2}{2} - \sum_{I=1}^{N} \frac{Z_I}{|\mathbf{r} - \mathbf{R_I}|} \right) \phi_q(\mathbf{x}),$$
$$h_{pqrs} = \int d\mathbf{x_1} d\mathbf{x_2} \frac{\phi_p^*(\mathbf{x_1}) \phi_q^*(\mathbf{x_2}) \phi_s(\mathbf{x_1}) \phi_r(\mathbf{x_2})}{|\mathbf{x_1} - \mathbf{x_2}|} \quad \text{(H2)}$$

are precalculated on classical computers by the Hartree-Fock method with $\mathcal{O}(K^4)$ scaling. Using the VQE method to compute the ground-state energy requires a parametrized ansatz or a trial wave function. Many different forms of wave functions are developed for such a purpose. A popular ansatz used by the VQE method is the unitary coupled-cluster ansatz with single and double excitations (UCCSD) [72] given by

$$\begin{aligned} |\Psi_{\mathrm{UCCSD}}(\theta)\rangle &= e^{\hat{T}_{\mathrm{SD}} + \hat{T}_{\mathrm{SD}}^\dagger} |\Psi_0\rangle \\ &= \exp\left[\sum_{ra} c_a^r (a_r^\dagger a_a - a_a^\dagger a_r) \right. \\ &\quad \left. + \sum_{a<b, r<s} c_{ab}^{rs} (a_r^\dagger a_s^\dagger a_a a_b - a_b^\dagger a_a^\dagger a_s a_r) \right] |\Psi_0\rangle, \end{aligned} \quad \text{(H3)}$$

where $\hat{T}_{\mathrm{SD}} = \hat{T}_1 + \hat{T}_2$ contains single- and double-excitation operators. $|\Psi_0\rangle$ is the ground-state wave function obtained by the Hartree-Fock method. Minimizing the expectation value of molecular energy $\langle \Psi_{\mathrm{UCCSD}}(\theta) | \hat{H}_0 | \Psi_{\mathrm{UCCSD}}(\theta) \rangle$, we find the ground-state wave function and the corresponding energy.

For a two-electron system equipped with STO-3G basis, it has four spin orbitals denoted by $g, \bar{g}, u, \bar{u}$ representing gerade spin-up, gerade spin-down, ungerade spin-up, and ungerade spin-down orbitals, respectively. It is evident that the two electrons occupy two of the four spin orbitals, and as a result, the ground-state function of the molecule stays in the linear space V spanned by the following four basis states [73]:

$$V = \{ |\sigma_g \bar{\sigma}_g\rangle, |\sigma_u \bar{\sigma}_u\rangle, |\sigma_g \bar{\sigma}_u\rangle, |\sigma_u \bar{\sigma}_g\rangle \}. \quad \text{(H4)}$$

For the H_2 molecule, the ground-state wave function $|\psi_{H_2}\rangle$ stays in a smaller linear space

$$V_g = \{ |\sigma_g \bar{\sigma}_g\rangle, |\sigma_u \bar{\sigma}_u\rangle \} \quad \text{(H5)}$$

due to its central symmetry. As a result, the electronic Hamiltonian (H1) for the two-electron system is simplified as

$$\begin{aligned} H = {} & h_{gg}(a_g^\dagger a_g + a_{\bar{g}}^\dagger a_{\bar{g}}) + h_{\mu\mu}(a_\mu^\dagger a_\mu + a_{\bar{\mu}}^\dagger a_{\bar{\mu}}) \\ & + h_{gg\mu\mu}(a_g^\dagger a_{\bar{g}}^\dagger a_{\bar{\mu}} a_\mu + a_g^\dagger a_{\bar{\mu}}^\dagger a_{\bar{g}} a_\mu + a_\mu^\dagger a_{\bar{g}}^\dagger a_{\bar{\mu}} a_g + a_\mu^\dagger a_{\bar{\mu}}^\dagger a_{\bar{g}} a_g) \\ & + (h_{g\mu g\mu} - h_{g\mu\mu g})(a_g^\dagger a_\mu^\dagger a_\mu a_g + a_{\bar{g}}^\dagger a_{\bar{\mu}}^\dagger a_{\bar{\mu}} a_{\bar{g}}) \\ & + h_{gggg} a_g^\dagger a_{\bar{g}}^\dagger a_g a_{\bar{g}} + h_{\mu\mu\mu\mu} a_\mu^\dagger a_{\bar{\mu}}^\dagger a_{\bar{\mu}} a_\mu \\ & + h_{g\mu g\mu}(a_g^\dagger a_{\bar{\mu}}^\dagger a_{\bar{\mu}} a_g + a_{\bar{g}}^\dagger a_\mu^\dagger a_\mu a_{\bar{g}}). \end{aligned}$$

To perform the VQE algorithm, we need to encode or map the ground-state wave function and the Hamiltonian into quantum circuits. There exist several schemes to encode the creation and annihilation operators into strings of Pauli gates. The common choices are the Jordan-Wigner, parity, and Bravyi-Kitaev transformations. In our simulation, we

employ the Bravyi-Kitaev (BK) transformation [74] to encode the wave functions and Hamiltonians, which enables the reduction of using two qubits for simulations or experiments through Z_2 symmetry.

For the two-electron system, we store the occupation numbers of spin orbitals $|\Phi_0\rangle$ in the order of $|f_{\bar{\sigma}_u}, f_{\bar{\sigma}_g}, f_{\sigma_u}, f_{\sigma_g}\rangle$, where f equals 1 (occupied) or 0 (unoccupied). In the following, we denote the order $\sigma_u, \sigma_g, \sigma_u$, and σ_g by 3,2,1, and 0 for simplicity. As a result, the indices in Hamiltonian (H1) and $|\Phi_0\rangle$ are modified. Under the BK transformation, the encoded wave function of two-electron system (H4) stays in the space $V_g^{\text{qubit}} = \{|0101\rangle, |1010\rangle, |0110\rangle, |1001\rangle\}$, or $= \{|11\rangle, |00\rangle, |10\rangle, |01\rangle\}$ under Z_2 reduction. The encoded wave function (H5) of H_2 stays in $V_u^{\text{qubit}} = \{|0101\rangle, |1010\rangle\}$, or $= \{|11\rangle, |00\rangle\}$ under Z_2 reduction.

After some calculation, the UCCSD operator of the two-electron system is found to take the following form:

$$U(\theta) = \exp[\theta_{10}(a_1^\dagger a_0 - a_0^\dagger a_1) + \theta_{32}(a_3^\dagger a_2 - a_2^\dagger a_3) + \theta_{3120}(a_3^\dagger a_1^\dagger a_0 a_2 - a_2^\dagger a_0^\dagger a_1 a_3)]. \tag{H6}$$

Carrying out the BK encoding, the UCCSD operator becomes

$$U(\theta) = \exp\left\{ i\left[\frac{\theta_{3120}}{2}(X_1Y_0 + Y_1X_0) + \frac{\theta_{10}}{2}Y_0 + \frac{\theta_{32}}{2}Y_1\right]\right\},$$

and the corresponding Hamiltonian becomes

$$H_{\text{HeH}^+}^{\text{BK}} = a_0 I + a_1 IZ + a_2 IX + a_3 ZI + a_4 XI + a_5 ZZ + a_6 ZX + a_7 XZ + a_8 XX. \tag{H7}$$

The single-excitation terms $a_1^\dagger a_0 - a_0^\dagger a_1$ and $a_3^\dagger a_2 - a_2^\dagger a_3$ are discarded for the H_2 molecule due to its spatial symmetry, and the resulting UCCSD operator is simplified into

$$U(\theta) = \exp\left[i\frac{\theta}{2}(X_1Y_0 + Y_1X_0)\right]. \tag{H8}$$

For the ground state of H_2 (state $|11\rangle$ under BK transformation with Z_2 symmetry), the ansatz and Hamiltonian are further simplified into

$$U(\theta)|11\rangle = e^{i\theta X_1Y_0}|11\rangle,$$
$$H_{\text{H}_2}^{\text{BK}} = a_0 I + a_1 Z_0 + a_2 Z_1 + a_3 Z_1Z_0 + a_4 X_1X_0. \tag{H9}$$

To evaluate the ground-state energy of the system, we need to compute the expected value of each term in $H_{\text{H}_2}^{\text{BK}}$, which is measured directly with quantum circuits.

2. Derivation of the UCCSD ansatz of H_2

The general form of the UCC operator is given by

$$U(\theta) = e^{T(\theta) - T^\dagger(\theta)}, \tag{H10}$$

where $T(\theta)$ is the excitation operator defined by full configuration interaction, and for most of the time, the UCCSD ansatz is sufficient to deal with this problem. As we mention above, we store the occupation numbers of spin orbitals ordered by $|f_{\bar{\sigma}_u}, f_{\bar{\sigma}_g}, f_{\sigma_u}, f_{\sigma_g}\rangle$. As a result, the initial state of H_2 (obtained through classical quantum-chemistry computation such as the Hartree-Fock method) in particle number representation is $|0101\rangle$. Accordingly, following the BK transformation, the initial state changes to $|0111\rangle$ (or $|11\rangle$ under Z_2 reduction). Thus, for H_2 with STO-3G basis, the operator is simplified into [72]

$$U(\theta) = e^{\theta_{3120}(a_3^\dagger a_1^\dagger a_0 a_2 - a_2^\dagger a_0^\dagger a_1 a_3)}. \tag{H11}$$

Following BK encoding, the fermionic operators are given by

$$\begin{aligned}
a_0^\dagger &= \frac{1}{2}X_3X_1X_0 - \frac{1}{2}iX_3X_1Y_0,\\
a_0 &= \frac{1}{2}X_3X_1X_0 + \frac{1}{2}iX_3X_1Y_0,\\
a_1^\dagger &= \frac{1}{2}X_3X_1Z_0 - \frac{1}{2}iX_3Y_1,\\
a_1 &= \frac{1}{2}X_3X_1Z_0 + \frac{1}{2}iX_3Y_1,\\
a_2^\dagger &= \frac{1}{2}X_3X_2Z_1 - \frac{1}{2}iX_3Y_2Z_1,\\
a_2 &= \frac{1}{2}X_3X_2Z_0 + \frac{1}{2}iX_3Y_2Z_1,\\
a_3^\dagger &= \frac{1}{2}X_3Z_2Z_1 - \frac{1}{2}iY_3,\\
a_3 &= \frac{1}{2}X_3Z_2Z_1 + \frac{1}{2}iY_3.
\end{aligned} \tag{H12}$$

For Pauli matrices (or Pauli gates), they satisfy the equalities $XX = YY = ZZ = 1, XY = -YX = iZ, YZ = -ZY = iX$, and $ZX = -XZ = iY$. Based on the above equations, it is easy to show that

$$\begin{aligned}
&a_3^\dagger a_1^\dagger a_0 a_2 - a_2^\dagger a_0^\dagger a_1 a_3\\
&= \frac{1}{8}i(Y_2X_0 + X_2Y_0 - Y_2Z_1X_0 + X_2Z_1Y_0 + Z_3X_2Z_1Y_0\\
&\quad - Z_3Y_2Z_1X_0 + Z_3X_2Y_0 + Z_3Y_2X_0).
\end{aligned} \tag{H13}$$

To omit the qubits 1 and 3 in $|0111\rangle$ by Z_2 symmetry, one needs to consider the effect of the Pauli matrices acting on qubits 1 and 3, when the remaining two qubits (i.e., qubits 0 and 4) are concerned. For the eight terms in the above

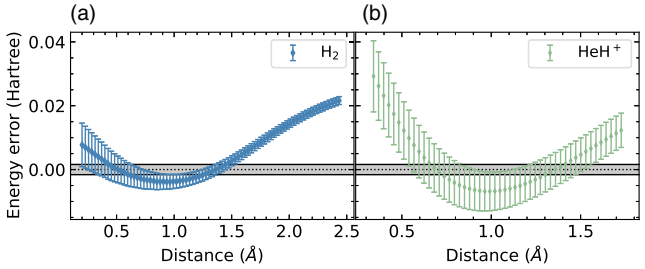

FIG. 12. The energy error and standard deviation for (a) H_2 and (b) HeH^+. The energy error is defined as the difference between the measured and exact energy, with the dotted line the expected error and the gray shadow region denoting the chemical accuracy of $\pm 1.6 \times 10^{-3}$ hartree. The error bars represent the standard deviation of the sample mean obtained by bootstrapping from 4096 projective measurement repetitions. The data points for H_2 are obtained from the Gaussian process regression on 50 different values for the variational parameter.

equation, only the Z matrix acts on the qubits 1 and 3. At the same time, it is evident that $Z_3|0111\rangle = |0111\rangle$ and $Z_1|0111\rangle = -|0111\rangle$. Thus, the form of $a_3^\dagger a_1^\dagger a_0 a_2 - a_2^\dagger a_0^\dagger a_1 a_3$ after Z_2 reduction becomes

$$a_3^\dagger a_1^\dagger a_0 a_2 - a_2^\dagger a_0^\dagger a_1 a_3 = \frac{1}{2}(X_2 Y_0 + Y_2 X_0), \tag{H14}$$

which, equivalently, can also be expressed as $\frac{1}{2}(X_1 Y_0 + Y_1 X_0)$, since qubit 1 is omitted (allowing us to renumber qubit 2 as 1). Therefore, the ansatz $U(\theta) = e^{\frac{1}{2}i\theta(X_1 Y_0 + Y_1 X_0)}$ is rewritten as $e^{\frac{1}{2}i\theta X_1 Y_0} e^{\frac{1}{2}i\theta Y_1 X_0}$. On the other hand, $e^{\frac{1}{2}i\theta X_1 Y_0}|11\rangle = e^{\frac{1}{2}i\theta Y_1 X_0}|11\rangle$ holds, and as a result the UCCSD ansatz of H_2 with STO-3G is recast as

$$U(\theta) = e^{i\theta X_1 Y_0}|11\rangle = e^{i\theta Y_1 X_0}|11\rangle. \tag{H15}$$

The results for the measured errors for energy with fluctuations for H_2 and HeH^+ are, respectively, shown in Fig. 12.

[1] D. Gottesman, *Fault-Tolerant Quantum Computation with Higher-Dimensional Systems*, Chaos Solitons Fractals **10**, 1749 (1999).

[2] Y. Wang, Z. Hu, B. C. Sanders, and S. Kais, *Qudits and High-Dimensional Quantum Computing*, Front. Phys. **8**, 589504 (2020).

[3] M. Ringbauer, M. Meth, L. Postler, R. Stricker, R. Blatt, P. Schindler, and T. Monz, *A Universal Qudit Quantum Processor with Trapped Ions*, Nat. Phys. **18**, 1053 (2022).

[4] M. Erhard, R. Fickler, M. Krenn, and A. Zeilinger, *Twisted Photons: New Quantum Perspectives in High Dimensions*, Light **7**, 17146 (2018).

[5] Y. Chi, J. Huang, Z. Zhang, J. Mao, Z. Zhou, X. Chen, C. Zhai, J. Bao, T. Dai, H. Yuan *et al.*, *A Programmable Qudit-Based Quantum Processor*, Nat. Commun. **13**, 1166 (2022).

[6] D. González-Cuadra, T. V. Zache, J. Carrasco, B. Kraus, and P. Zoller, *Hardware Efficient Quantum Simulation of Non-Abelian Gauge Theories with Qudits on Rydberg Platforms*, Phys. Rev. Lett. **129**, 160501 (2022).

[7] T. Vértesi, S. Pironio, and N. Brunner, *Closing the Detection Loophole in Bell Experiments Using Qudits*, Phys. Rev. Lett. **104**, 060401 (2010).

[8] H.-P. Lo, C.-M. Li, A. Yabushita, Y.-N. Chen, C.-W. Luo, and T. Kobayashi, *Experimental Violation of Bell Inequalities for Multi-Dimensional Systems*, Sci. Rep. **6**, 22088 (2016).

[9] N. J. Cerf, M. Bourennane, A. Karlsson, and N. Gisin, *Security of Quantum Key Distribution Using d-Level Systems*, Phys. Rev. Lett. **88**, 127902 (2002).

[10] M. Bergmann and P. van Loock, *Hybrid Quantum Repeater for Qudits*, Phys. Rev. A **99**, 032349 (2019).

[11] Y. Shen, X. Zhang, S. Zhang, J.-N. Zhang, M.-H. Yung, and K. Kim, *Quantum Implementation of the Unitary Coupled Cluster for Simulating Molecular Electronic Structure*, Phys. Rev. A **95**, 020501(R) (2017).

[12] P. J. Low, B. M. White, A. A. Cox, M. L. Day, and C. Senko, *Practical Trapped-Ion Protocols for Universal Qudit-Based Quantum Computing*, Phys. Rev. Res. **2**, 033128 (2020).

[13] E. Munro, A. Asenjo-Garcia, Y. Lin, L. C. Kwek, C. A. Regal, and D. E. Chang, *Population Mixing Due to Dipole-Dipole Interactions in a One-Dimensional Array of Multilevel Atoms*, Phys. Rev. A **98**, 033815 (2018).

[14] A. Babazadeh, M. Erhard, F. Wang, M. Malik, R. Nouroozi, M. Krenn, and A. Zeilinger, *High-Dimensional Single-Photon Quantum Gates: Concepts and Experiments*, Phys. Rev. Lett. **119**, 180510 (2017).

[15] P. Imany, J. A. Jaramillo-Villegas, M. S. Alshaykh, J. M. Lukens, O. D. Odele, A. J. Moore, D. E. Leaird, M. Qi, and A. M. Weiner, *High-Dimensional Optical Quantum Logic in Large Operational Spaces*, npj Quantum Inf. **5**, 59 (2019).

[16] M. Kues, C. Reimer, P. Roztocki, L. R. Cortés, S. Sciara, B. Wetzel, Y. Zhang, A. Cino, S. T. Chu, B. E. Little *et al.*, *On-Chip Generation of High-Dimensional Entangled Quantum States and Their Coherent Control*, Nature (London) **546**, 622 (2017).

[17] N. T. Islam, C. C. W. Lim, C. Cahall, J. Kim, and D. J. Gauthier, *Provably Secure and High-Rate Quantum Key Distribution with Time-Bin Qudits*, Sci. Adv. **3**, e1701491 (2017).

[18] P. C. Humphreys, B. J. Metcalf, J. B. Spring, M. Moore, X.-M. Jin, M. Barbieri, W. S. Kolthammer, and I. A. Walmsley, *Linear Optical Quantum Computing in a Single Spatial Mode*, Phys. Rev. Lett. **111**, 150501 (2013).

[19] M. R. A. Adcock, P. Høyer, and B. C. Sanders, *Quantum Computation with Coherent Spin States and the Close Hadamard Problem*, Quantum Inf. Process. **15**, 1361 (2016).

[20] Y. Fu, W. Liu, X. Ye, Y. Wang, C. Zhang, C.-K. Duan, X. Rong, and J. Du, *Experimental Investigation of Quantum Correlations in a Two-Qutrit Spin System*, Phys. Rev. Lett. **129**, 100501 (2022).

[21] S. Choi, N. Y. Yao, and M. D. Lukin, *Dynamical Engineering of Interactions in Qudit Ensembles*, Phys. Rev. Lett. **119**, 183603 (2017).

[22] S. Dogra, Arvind, and K. Dorai, *Determining the Parity of a Permutation Using an Experimental NMR Qutrit*, Phys. Lett. A **378**, 3452 (2014).

[23] H.-Y. Huang, M. Broughton, J. Cotler, S. Chen, J. Li, M. Mohseni, H. Neven, R. Babbush, R. Kueng, J. Preskill, and J. R. McClean, *Quantum Advantage in Learning from Experiments*, Science **376**, 1182 (2022).

[24] P. J. J. O'Malley, R. Babbush, I. D. Kivlichan, J. Romero, J. R. McClean, R. Barends, J. Kelly, P. Roushan, A. Tranter, N. Ding *et al.*, *Scalable Quantum Simulation of Molecular Energies*, Phys. Rev. X **6**, 031007 (2016).

[25] W. J. Huggins, B. A. O'Gorman, N. C. Rubin, D. R. Reichman, R. Babbush, and J. Lee, *Unbiasing Fermionic Quantum Monte Carlo with a Quantum Computer*, Nature (London) **603**, 416 (2022).

[26] K. J. Satzinger, Y. J. Liu, A. Smith, C. Knapp, M. Newman, C. Jones, Z. Chen, C. Quintana, X. Mi, A. Dunsworth *et al.*, *Realizing Topologically Ordered States on a Quantum Processor*, Science **374**, 1237 (2021).

[27] S. Krinner, N. Lacroix, A. Remm, A. Di Paolo, E. Genois, C. Leroux, C. Hellings, S. Lazar, F. Swiadek, J. Herrmann *et al.*, *Realizing Repeated Quantum Error Correction in a Distance-Three Surface Code*, Nature (London) **605**, 669 (2022).

[28] F. Arute, K. Arya, R. Babbush, D. Bacon, J. C. Bardin, R. Barends, R. Biswas, S. Boixo, F. o. Brandao *et al.*, *Quantum Supremacy Using a Programmable Superconducting Processor*, Nature (London) **574**, 505 (2019).

[29] J. Koch, T. M. Yu, J. Gambetta, A. A. Houck, D. I. Schuster, J. Majer, A. Blais, M. H. Devoret, S. M. Girvin, and R. J. Schoelkopf, *Charge-Insensitive Dubit Design Derived from the Cooper Pair Box*, Phys. Rev. A **76**, 042319 (2007).

[30] F. W. Strauch, P. R. Johnson, A. J. Dragt, C. J. Lobb, J. R. Anderson, and F. C. Wellstood, *Quantum Logic Gates for Coupled Superconducting Phase Qubits*, Phys. Rev. Lett. **91**, 167005 (2003).

[31] C. Rigetti and M. Devoret, *Fully Microwave-Tunable Universal Gates in Superconducting Qubits with Linear Couplings and Fixed Transition Frequencies*, Phys. Rev. B **81**, 134507 (2010).

[32] J. Chu, X. He, Y. Zhou, J. Yuan, L. Zhang, Q. Guo, Y. Hai, Z. Han, C.-K. Hu, W. Huang *et al.*, *Scalable Algorithm Simplification Using Quantum and Logic*, Nat. Phys. **19**, 126 (2023).

[33] B. G. U. Englert, G. Mangano, M. Mariantoni, R. Gross, J. Siewert, and E. Solano, *Mesoscopic Shelving Readout of Superconducting Qubits in Circuit Quantum Electrodynamics*, Phys. Rev. B **81**, 134514 (2010).

[34] S. S. Elder, C. S. Wang, P. Reinhold, C. T. Hann, K. S. Chou, B. J. Lester, S. Rosenblum, L. Frunzio, L. Jiang, and R. J. Schoelkopf, *High-Fidelity Measurement of Qubits Encoded in Multilevel Superconducting Circuits*, Phys. Rev. X **10**, 011001 (2020).

[35] E. O. Kiktenko, A. K. Fedorov, O. V. Man'ko, and V. I. Man'ko, *Multilevel Superconducting Circuits as Two-Qubit Systems: Operations, State Preparation, and Entropic Inequalities*, Phys. Rev. A **91**, 042312 (2015).

[36] R. Bianchetti, S. Filipp, M. Baur, J. M. Fink, C. Lang, L. Steffen, M. Boissonneault, A. Blais, and A. Wallraff, *Control and Tomography of a Three Level Superconducting Artificial Atom*, Phys. Rev. Lett. **105**, 223601 (2010).

[37] A. Cervera-Lierta, M. Krenn, A. Aspuru-Guzik, and A. Galda, *Experimental High-Dimensional Greenberger-Horne-Zeilinger Entanglement with Superconducting Transmon Qutrits*, Phys. Rev. Appl. **17**, 024062 (2022).

[38] T. Brown, E. Doucet, D. Ristè, G. Ribeill, K. Cicak, J. Aumentado, R. Simmonds, L. Govia, A. Kamal, and L. Ranzani, *Trade Off-Free Entanglement Stabilization in a Superconducting Qutrit-Qubit System*, Nat. Commun. **13**, 3994 (2022).

[39] M. S. Blok, V. V. Ramasesh, T. Schuster, K. O'Brien, J. M. Kreikebaum, D. Dahlen, A. Morvan, B. Yoshida, N. Y. Yao, and I. Siddiqi, *Quantum Information Scrambling on a Superconducting Qutrit Processor*, Phys. Rev. X **11**, 021010 (2021).

[40] H. K. Xu, C. Song, W. Y. Liu, G. M. Xue, F. F. Su, H. Deng, Y. Tian, D. N. Zheng, S. Han, Y. P. Zhong *et al.*, *Coherent Population Transfer between Uncoupled or Weakly Coupled States in Ladder-Type Superconducting Qutrits*, Nat. Commun. **7**, 11018 (2016).

[41] K. Luo, W. Huang, Z. Tao, L. Zhang, Y. Zhou, J. Chu, W. Liu, B. Wang, J. Cui, S. Liu *et al.*, *Experimental Realization of Two Qutrits Gate with Tunable Coupling in Superconducting Circuits*, Phys. Rev. Lett. **130**, 030603 (2023).

[42] N. Goss, A. Morvan, B. Marinelli, B. K. Mitchell, L. B. Nguyen, R. K. Naik, L. Chen, C. Jünger, J. M. Kreikebaum, D. I. Santiago *et al.*, *High-Fidelity Qutrit Entangling Gates for Superconducting Circuits*, Nat. Commun. **13**, 7481 (2022).

[43] W. Zheng, Y. Zhang, Y. Dong, J. Xu, Z. Wang, X. Wang, Y. Li, D. Lan, J. Zhao, S. Li *et al.*, *Optimal Control of Stimulated Raman Adiabatic Passage in a Superconducting Qudit*, npj Quantum Inf. **8**, 9 (2022).

[44] M. J. Peterer, S. J. Bader, X. Jin, F. Yan, A. Kamal, T. J. Gudmundsen, P. J. Leek, T. P. Orlando, W. D. Oliver, and S. Gustavsson, *Coherence and Decay of Higher Energy Levels of a Superconducting Transmon Qubit*, Phys. Rev. Lett. **114**, 010501 (2015).

[45] D. M. Tennant, L. A. Martinez, C. D. Wilen, R. McDermott, J. L. DuBois, and Y. J. Rosen, *Low-Frequency Correlated Charge-Noise Measurements across Multiple Energy Transitions in a Tantalum Transmon*, PRX Quantum **3**, 030307 (2022).

[46] F. A. Bonk, R. S. Sarthour, E. R. deAzevedo, J. D. Bulnes, G. L. Mantovani, J. C. C. Freitas, T. J. Bonagamba, A. P. Guimarães, and I. S. Oliveira, *Quantum-State Tomography for Quadrupole Nuclei and Its Application on a Two-Qubit System*, Phys. Rev. A **69**, 042322 (2004).

[47] D. C. McKay, C. J. Wood, S. Sheldon, J. M. Chow, and J. M. Gambetta, *Efficient z Gates for Quantum Computing*, Phys. Rev. A **96**, 022330 (2017).

[48] A. Barenco, C. H. Bennett, R. Cleve, D. P. DiVincenzo, N. Margolus, P. Shor, T. Sleator, J. A. Smolin, and H. Weinfurter, *Elementary Gates for Quantum Computation*, Phys. Rev. A **52**, 3457 (1995).

[49] M. A. Nielsen and I. L. Chuang, *Quantum Computation and Quantum Information*, 10th ed. (Cambridge University Press, Cambridge, England, 2010).

[50] D. P. O'Leary, G. K. Brennen, and S. S. Bullock, *Parallelism for Quantum Computation with Qudits*, Phys. Rev. A **74**, 032334 (2006).
[51] I. J. Myung, *Tutorial on Maximum Likelihood Estimation*, J. Math. Psychol. **47**, 90 (2003).
[52] G. C. Knee, E. Bolduc, J. Leach, and E. M. Gauger, *Quantum Process Tomography via Completely Positive and Trace-preserving Projection*, Phys. Rev. A **98**, 062336 (2018).
[53] T. Abad, J. Fernández-Pendás, A. Frisk Kockum, and G. Johansson, *Universal Fidelity Reduction of Quantum Operations from Weak Dissipation*, Phys. Rev. Lett. **129**, 150504 (2022).
[54] R. Blume-Kohout, J. K. Gamble, E. Nielsen, K. Rudinger, J. Mizrahi, K. Fortier, and P. Maunz, *Correction: Publisher Correction: Demonstration of Qubit Operations below a Rigorous Fault Tolerance Threshold with Gate Set Tomography*, Nat. Commun. **9**, 16226 (2018).
[55] D. Greenbaum, *Introduction to Quantum Gate Set Tomography*, arXiv:1509.02921.
[56] Z. Gedik, I. A. Silva, B. Çakmak, G. Karpat, E. L. G. Vidoto, D. O. Soares-Pinto, E. R. deAzevedo, and F. F. Fanchini, *Computational Speed-Up with a Single Qudit*, Sci. Rep. **5**, 14671 (2015).
[57] L. K. Grover, *Quantum Mechanics Helps in Searching for a Needle in a Haystack*, Phys. Rev. Lett. **79**, 325 (1997).
[58] F. M. Toyama, W. van Dijk, and Y. Nogami, *Quantum Search with Certainty Based on Modified Grover Algorithms: Optimum Choice of Parameters*, Quantum Inf. Process. **12**, 1897 (2013).
[59] G. L. Long, *Grover Algorithm with Zero Theoretical Failure Rate*, Phys. Rev. A **64**, 022307 (2001).
[60] J. Preskill, *Quantum Computing in the NISQ Era and Beyond*, Quantum **2**, 79 (2018).
[61] A. Peruzzo, J. McClean, P. Shadbolt, M.-H. Yung, X.-Q. Zhou, P. J. Love, A. Aspuru-Guzik, and J. L. O'Brien, *A Variational Eigenvalue Solver on a Photonic Quantum Processor*, Nat. Commun. **5**, 4213 (2014).
[62] L. Martinez, Z. Peng, D. Appelö, D. Tennant, N. A. Petersson, J. DuBois, and Y. Rosen, *Noise-Specific Beats in the Higher-Level Ramsey Curves of a Transmon Qubit*, Appl. Phys. Lett. **122**, 114002 (2023).
[63] L. E. Fischer, A. Chiesa, F. Tacchino, D. J. Egger, S. Carretta, and I. Tavernelli, *Towards Universal Gate Synthesis and Error Correction in Transmon Qudits*, arXiv:2212.04496.
[64] S. Cao, D. Lall, M. Bakr, G. Campanaro, S. Fasciati, J. Wills, V. Chidambaram, B. Shteynas, I. Rungger, and P. Leek, *Efficient Qutrit Gate-Set Tomography on a Transmon*, arXiv:2210.04857.
[65] T. Roy, Z. Li, E. Kapit, and D. I. Schuster, *Realization of Two-Qutrit Quantum Algorithms on a Programmable Superconducting Processor*, arXiv:2211.06523.
[66] K. Mato, M. Ringbauer, S. Hillmich, and R. Wille, *Compilation of Entangling Gates for High-Dimensional Quantum Systems*, 10.1145/3566097.3567930 (2023).
[67] D. Janković, J.-G. Hartmann, M. Ruben, and P.-A. Hervieux, *Noisy Qudit vs Multiple Qubits: Conditions on Gate Efficiency*, arXiv:2302.04543.
[68] C. Wang, X. Li, H. Xu, Z. Li, J. Wang, Z. Yang, Z. Mi, X. Liang, T. Su, C. Yang *et al.*, *Towards Practical Quantum Computers: Transmon Qubit with a Lifetime Approaching 0.5 Milliseconds*, npj Quantum Inf. **8**, 3 (2022).
[69] J. M. Gambetta, F. Motzoi, S. T. Merkel, and F. K. Wilhelm, *Analytic Control Methods for High-Fidelity Unitary Operations in a Weakly Nonlinear Oscillator*, Phys. Rev. A **83**, 012308 (2011).
[70] T. H. Cormen, C. E. Leiserson, R. L. Rivest, and C. Stein, *Introduction to Algorithms* (MIT Press, Cambridge, MA, 2022).
[71] S. McArdle, S. Endo, A. Aspuru-Guzik, S. C. Benjamin, and X. Yuan, *Quantum Computational Chemistry*, Rev. Mod. Phys. **92**, 015003 (2020).
[72] C. Hempel, C. Maier, J. Romero, J. McClean, T. Monz, H. Shen, P. Jurcevic, B. P. Lanyon, P. Love, R. Babbush *et al.*, *Quantum Chemistry Calculations on a Trapped-Ion Quantum Simulator*, Phys. Rev. X **8**, 031022 (2018).
[73] K. Huang, X. Cai, H. Li, Z.-Y. Ge, R. Hou, H. Li, T. Liu, Y. Shi, C. Chen, D. Zheng *et al.*, *Variational Quantum Computation of Molecular Linear Response Properties on a Superconducting Quantum Processor*, J. Phys. Chem. Lett. **13**, 9114 (2022).
[74] J. T. Seeley, M. J. Richard, and P. J. Love, *The Bravyi-Kitaev Transformation for Quantum Computation of Electronic Structure*, J. Chem. Phys. **137**, 224109 (2012).